

**High Precision Calculation of Generic Extreme
Mass Ratio Inspirals**

by
William Throwe

Submitted to the Department of Physics
in partial fulfillment of the requirements for the degree of
Bachelor of Science in Physics

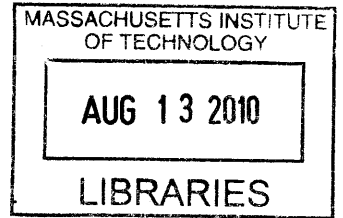
at the

MASSACHUSETTS INSTITUTE OF TECHNOLOGY

June 2010*

© William Throwe, MMX. All rights reserved.

The author hereby grants to MIT permission to reproduce and
distribute publicly paper and electronic copies of this thesis document
in whole or in part.

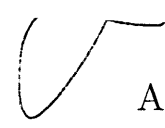


ARCHIVES


Author

Department of Physics
May 7, 2010

Certified by


Scott A. Hughes
Associate Professor
Thesis Supervisor

Accepted by


David E. Pritchard
Senior Thesis Coordinator, Department of Physics

High Precision Calculation of Generic Extreme Mass Ratio Inspirals

by

William Throwe

Submitted to the Department of Physics
on May 7, 2010, in partial fulfillment of the
requirements for the degree of
Bachelor of Science in Physics

Abstract

Orbits around black holes evolve due to gravitational-wave emission, losing energy and angular momentum, and driving the orbiting body to slowly spiral into the black hole. Recent theoretical advances now make it possible to model the impact of this wave emission on generic (eccentric and inclined) black hole orbits, allowing us to push beyond the handful of constrained (circular or equatorial) cases that previous work considered. This thesis presents the first systematic study of how generic black hole orbits evolve due to gravitational-wave emission. In addition to extending the class of orbits which can be analyzed, we also introduce a new formalism for solving for the wave equation which describes radiative backreaction. This approach is based on a spectral decomposition of the radiation field originally introduced by Mano, Suzuki, and Takasugi (MST), and was then adapted for numerical analysis by Fujita and Tagoshi (FT). We find that the MST-FT formalism allows us to compute various quantities significantly more accurately than previous work, even in strong field regimes. We use this code to explore the location in orbital parameter space of the surface at which the evolution of orbital eccentricity changes sign from negative (orbits circularize) to positive (orbits become more eccentric).

Thesis Supervisor: Scott A. Hughes
Title: Associate Professor

Acknowledgments

I would like to thank Professor Scott Hughes, my thesis advisor, for providing me with the perfect balance of guidance and freedom during my time as his student. I would also like to thank my parents for nurturing and encouraging my love of physics for longer than I can remember.

Contents

1	General Relativity and Black Holes	9
1.1	From Newton to Einstein	9
1.2	Black Holes	11
1.3	Orbits	12
1.4	Gravitational Waves	15
2	The Mathematics of Inspirals	19
2.1	The Teukolsky Formalism	19
2.2	Evolution of “Constants” of Motion	21
2.2.1	Energy and Angular Momentum	22
2.2.2	Carter Constant	23
3	The MST Formalism and Fujita and Tagoshi’s Method	25
3.1	The MST Formalism	25
3.2	Numerical MST	27
3.3	Solving the Continued Fraction Equation	29
4	Implementation	33
4.1	Numerical Precision	33
4.2	Algorithms and Truncation	34
5	Results	37
5.1	Comparison with Sasaki-Nakamura	37
5.1.1	Speed Comparisons	38

5.1.2 Precision Comparisons	40
5.2 Comparison with Previous Results	42
5.3 The $\dot{e} = 0$ Surface	44
6 Conclusions and Future Work	51
A Orbital Details	53
B Expressions for MST Quantities	55
C List of Symbols	59

Chapter 1

General Relativity and Black Holes

General Relativity, first formulated by Einstein and published in 1915, is currently our best description of gravity and the universe on large scales. It successfully describes everything from the orbits of planets in the solar system to the history of the universe as a whole. Perhaps its most well-known prediction, however, is the existence of black holes, objects with gravity so strong that nothing, not even light, can escape.

1.1 From Newton to Einstein

Until the 20th century, the best description of gravity available was the Newtonian one, which described a force acting between massive particles given by the familiar inverse square law

$$\mathbf{F} = -\frac{Gm_1m_2}{r^2}\hat{\mathbf{r}} \quad (1.1)$$

where m_1 and m_2 are the masses of the particles, \mathbf{r} is the vector separating them, and G is a constant. This, along with Newton's second law, described the motion of bodies under the influence of gravity.

With Einstein's discovery of Special Relativity in 1905, however, this description was seen to be incomplete. Special Relativity predicted that there was no universally preferred reference frame, that is, that two observers moving uniformly with respect to one another should have no method to decide which (if either) of them was at rest.

Additionally, it predicted that such observers disagree on the relative time between events at different locations in space. This poses a problem for any theory that requires action at a distance, because such theories are generally expressed in terms of the locations of bodies at a particular time. If different observers cannot agree on what it means for separated events to happen at the same time, then the theory's formulation doesn't make sense in Special Relativity.

Gravity needed, then to be reformulated in a manner not requiring long-distance forces. An idea for how to achieve this can be taken from Maxwell: we need a field to cause the force. While this concept is easy to describe, the details turn out to be much more complicated than in the case of electromagnetic fields. In fact, the field needed is not something that exists in space, but the shape of spacetime itself. A description of a gravitating system under General Relativity is a mathematical description of the geometry of spacetime, written as a metric. The metric is a measure of the distances between nearby points and obeys the Einstein Field Equations

$$G_{\mu\nu} = \frac{8\pi G}{c^4} T_{\mu\nu} \quad (1.2)$$

where $G_{\mu\nu}$ is a complicated second order differential operator acting on the metric, $T_{\mu\nu}$ is a description of the matter in the space, c is the speed of light, and G is the same constant that occurred in Newton's force law. This is a system of equations, as μ and ν are indices which run over the integers from 0 to 3. Kindly, we have the restriction that swapping μ and ν leaves the system of equations unchanged, so the Einstein Field Equations work out to be a system of ten coupled second order differential equations.

For convenience in calculations, it is traditional to choose units in which c and G are both 1. Under this convention, distances, times, masses, and energies are all measured in the same units, and the Einstein Field Equations become just

$$G_{\mu\nu} = 8\pi T_{\mu\nu}. \quad (1.3)$$

For the rest of this document, I will follow convention and use this "natural" unit

system. To gain some intuition about the magnitudes of quantities expressed in this way, note that the mass of the sun is

$$1 M_{\odot} = 1.47 \text{ km} = 4.92 \times 10^{-6} \text{ seconds.} \quad (1.4)$$

1.2 Black Holes

Solving the Field Equations is, not surprisingly, incredibly difficult. The only cases where we have analytic solutions of them are for very simple systems, with lots of symmetry. The simplest of these systems are black holes, which, in their most general form, are described by just three real numbers: mass, spin, and charge. As there are no large separations of charge observed in the universe, I will consider only uncharged black holes here.

The first black hole solution was found by Karl Schwarzschild in 1916. It described a static, spherically symmetric body in an otherwise empty universe. The Schwarzschild metric has only one parameter: the mass of the black hole, M , and is given by

$$ds^2 = - \left(1 - \frac{2M}{r} \right) dt^2 + \left(1 - \frac{2M}{r} \right)^{-1} dr^2 + r^2 (d\theta^2 + \sin^2 \theta d\varphi^2). \quad (1.5)$$

The coordinate t is the time, the quantities θ , and φ are the usual colatitude and longitude, and r labels a spherical surface of area $4\pi r^2$. Given the differences dt , dr , $d\theta$, and $d\varphi$ in t , r , θ , and φ , respectively, between two closely separated events, the metric gives the actual distance ds between them, measured by an observer claiming they are simultaneous.

The Schwarzschild metric has an interesting feature: the first two coefficients become zero and infinite at $r = 2M$. This suggests that something interesting happens at that radius, and indeed it is found that the solution has what is known as an event horizon there, through which stuff, be it matter, radiation, or information in general, can pass inwards, but not outwards.

The Schwarzschild solution is, however, too simple to describe objects that ac-

tually exist in our universe. Everything we know of is spinning, sometimes slowly, sometime very rapidly, and therefore has a spin axis and angular momentum, providing a preferred direction on that object. The perfect spherical symmetry of the Schwarzschild solution means that it cannot be a description of a spinning object, and must have no angular momentum. Finding the description of spinning black holes was a significantly harder challenge than the nonspinning case, and was only accomplished in 1963 by Roy Kerr. The Kerr metric is given (in Boyer-Lindquist coordinates) by

$$ds^2 = - \left(1 - \frac{2Mr}{\Sigma} \right) dt^2 + \frac{\Sigma}{\Delta} dr^2 + \Sigma d\theta^2 + \left(r^2 + a^2 + \frac{2Ma^2r}{\Sigma} \sin^2 \theta \right) \sin^2 \theta d\varphi^2 - \frac{4Mar}{\Sigma} \sin^2 \theta dt d\varphi \quad (1.6)$$

where $\Delta = r^2 - 2Mr + a^2$ and $\Sigma = r^2 + a^2 \cos^2 \theta$. As before, t is the time, r , θ , and φ specify a point in something similar to spherical coordinates, and M is the mass of the hole, but we now have a second parameter, a , which is the angular momentum per unit mass J/M . It can vary only in the range $-M < a < M$, and it is therefore often useful to introduce the dimensionless quantity $q = a/M$ which can vary from -1 to 1.

The Kerr metric shares many of the properties of the Schwarzschild solution. It has an event horizon, although it is at a slightly different radius of $r_+ = M + \sqrt{M^2 - a^2}$ (the larger root of $\Delta = 0$). Additionally, near the event horizon, space is warped in such a manner that everything must move around the hole in the same direction as its spin. This region, where nothing can stay at the same spatial coordinates, is known as the ergosphere. It extends out to $r = 2M$ at the equator and touches the event horizon at the poles.

1.3 Orbits

Consider a small particle of mass μ orbiting a heavy body of mass M . In Newtonian gravity, the particle will follow a simple periodic elliptical trajectory. It takes six

parameters (for example, the three components of each of the initial position and velocity) to completely specify the motion of a particle in orbit. Over long time scales, the initial position along the orbit is unimportant, so we can ignore one of the parameters, and are left with a Newtonian orbit described by five numbers. A common choice for these parameters are the semilatus rectum p , eccentricity e , inclination θ_{\min} , and two angles describing the orientation of the orbital plane and the direction of periapse. For an equatorial orbit, the radius as a function of angle is determined (up to a phase) by p and e as

$$r = \frac{p}{1 + e \cos \varphi}, \quad (1.7)$$

so the minimum and maximum radii are

$$r_{\min} = \frac{p}{1 + e} \quad r_{\max} = \frac{p}{1 - e}. \quad (1.8)$$

The three angular parameters rotate this ellipse to an arbitrary orientation, providing the most general orbit.

Not surprisingly, when we abandoned the simple equations of Newton for the nonlinear Einstein Field Equations, we also lost the simple forms of orbits. For orbits at large radius, the trajectories closely resemble the Newtonian paths, except that the ellipses do not quite close after each orbit. The direction of periapse and the plane of the orbit slowly precess, and, over a long period of time, the trajectory fills out a volume in space, rather than a curve. The last two angles listed above are no longer constants of motion, but become just part of the specification of the initial position of the particle in the orbit, which we do not care about on long timescales. Orbits in General Relativity are therefore described by three parameters.

Of course, when we are not far from the central object, the orbits will not look anything like ellipses. They will still, however, be bounded by an inner radius r_{\min} , an outer radius r_{\max} and a minimum angle away from the spin axis θ_{\min} . It is convenient to define a semilatus rectum and eccentricity by requiring that (1.8) are satisfied. This gives us one way of parametrizing the orbit: p, e, θ_{\min} .

Of course, there are other useful parametrizations. The Kerr metric (1.6) does

not depend on t or φ , so by Noether's theorem there are two conserved quantities in the system. In nonrelativistic systems, these quantities would be the energy E and angular momentum L , and this identification carries over very naturally to relativistic orbits as well. It turns out that there is another conserved quantity of a similar form to energy and angular momentum, but not related to a simple symmetry of the Kerr metric. This constant is called the Carter constant and denoted Q . It will be convenient to divide E , L , and Q by appropriate powers of the masses M and μ so as to make them dimensionless (see Appendix A for explicit expressions).

While distant orbits resemble those from Newtonian gravity with some small corrections, orbits passing very close to a black hole are grossly different. For highly eccentric orbits, the orbiting particle will (as in the Newtonian case) spend most of its orbital period far from the black hole, but on the close part of the orbit it may circle the hole several times before returning to large radius. This is sometimes poetically referred to as a “zoom-whirl” orbit. In an even more serious departure from familiar behavior, for small enough values of p the orbit actually becomes unstable and the particle plunges into the central black hole. For a given eccentricity and inclination, the semilatus rectum at which this plunge occurs is called the innermost stable orbit.

As the motion of the orbiting particle is no longer confined to a line, the description of motion along an orbit changes from a differential equation for $d\varphi/dt$ with φ as in (1.7) to a set of three coupled differential equations for dr/dt , $d\theta/dt$, and $d\varphi/dt$. However, by changing the time variable to “Mino time” λ [10], these equations decouple (although we gain another describing the rate of change of λ) to give

$$\begin{aligned} \left(\frac{dr}{d\lambda}\right)^2 &= V_r(r) & \frac{dt}{d\lambda} &= V_t(r, \theta) \\ \left(\frac{d\theta}{d\lambda}\right)^2 &= V_\theta(\theta) & \frac{d\varphi}{d\lambda} &= V_\varphi(r, \theta) \end{aligned} \quad (1.9)$$

where the four V functions (given in Appendix A) are functions only of the explicitly mentioned variables and the orbital parameters. This shows that r and θ are in fact periodic functions of λ . The Mino time frequencies of these orbits are often useful

and are denoted Υ_r and Υ_θ . Using the solutions for r and θ as functions of λ , we can see that V_φ and V_t are biperiodic functions with these frequencies. We can average V_φ and V_t over many periods of the r and θ oscillations and obtain an average rate of advancement for φ and t , which we denote Υ_φ and Γ , respectively.

Of course, measurements by a distant observer are done in Boyer-Lindquist time t , not Mino time λ , so for observations it is more useful to convert the frequencies to Boyer-Lindquist time frequencies as

$$\Omega_r = \frac{\Upsilon_r}{\Gamma} \qquad \Omega_\theta = \frac{\Upsilon_\theta}{\Gamma} \qquad \Omega_\varphi = \frac{\Upsilon_\varphi}{\Gamma}. \qquad (1.10)$$

When observing orbits from large radius, we will see the coordinates r and θ as periodic functions with frequencies Ω_r and Ω_θ and the derivative $d\varphi/dt$ as a biperiodic function with these frequencies. As the φ coordinate is periodic, we will observe the orbit's φ coordinate to be a triperiodic function with frequencies Ω_r , Ω_θ , and Ω_φ . Interesting observables should be expressible in terms of the r , θ , and φ coordinates of the particle, and so will also be triperiodic functions of time. If we Fourier transform any such observable, we should see contributions only from frequencies given by

$$\omega_{mkn} = m\Omega_\varphi + k\Omega_\theta + n\Omega_r. \qquad (1.11)$$

1.4 Gravitational Waves

Returning to the reformulation of gravity discussed in Section 1.1, we can look for new predictions unrelated to the very strong field properties of black holes. Recall that General Relativity posits a new field through which information propagates at a finite speed, similar to the electromagnetic field. Although the Einstein Field Equations are much more complicated than Maxwell's equations for electromagnetism, we can hope to draw useful analogies between the gravitational and electromagnetic fields.¹ One of the most notable properties of the electromagnetic field is that it admits propagating

¹These analogies can be made rigorous for weak fields in otherwise flat spacetime. See, for example, Chapter 7 of Carroll [1].

wave solutions, physically manifested as visible light, so we should look for similar effects in General Relativity.

Such propagating wave solutions do, in fact, exist. For small amplitude waves, we can ignore the nonlinear parts of the field equations and find sinusoidal solutions, traveling at the speed of light. Just like electromagnetic waves, gravitational waves carry energy and momentum. Also, just as an accelerating electric charge produces electromagnetic waves, an accelerating mass produces gravitational waves.

Also similar to electromagnetic waves, we find that gravitational waves come in two polarizations, conventionally called “plus” and “cross.” These polarizations do not, however, look like the electromagnetic polarizations. While electromagnetic waves can be described by oscillating electric field vectors, gravitational waves are best described as stretching and compressing space in directions perpendicular to their motion: one direction is stretched while the direction perpendicular to it is compressed, and then half a period later the directions have switched. In the plus polarization the directions of stretching line up with the coordinate axes, while in the cross polarization they are rotated by 45 degrees.

Recall, however, that the observation that accelerating charges produce waves which carry off energy implied the instability of the classical atom. The same argument holds for two bodies orbiting under a gravitational attraction, and for large systems we cannot appeal to quantum mechanics to restore the stability of the orbit. General Relativity predicts that gravitationally bound systems are unstable, and an orbiting particle will eventually spiral into the central mass.

Of course, the solar system has existed for billions of years, so clearly this inspiral is quite slow except for extremely close orbits. Inspiral was, however, observed in a tight neutron star binary by Hulse and Taylor, for which they received the 1993 Nobel Prize, and since their original observation several other inspiraling systems have been observed. Additionally, inspirals towards black holes are expected to be a major source of the gravitational waves detected by LIGO and LISA.

In this paper, I will focus only on systems where the central body is much more massive than the orbiting particle. Inspirals in such systems, known as Extreme Mass

Ratio Inspirals (EMRIs), allow for significant simplification of the general inspiral problem. The large central body can be approximated as unaffected by the orbiting body, and the nonlinear effects in the radiation from the orbiting particle can be neglected.

In the weak field regime far from the central body, orbits are almost those predicted by Newtonian gravity. As the gravitational waves are expected to be produced more energetically when the orbiting particle is under larger accelerations, such as near periapse, we expect the orbit to tend to circularize over time. In this regime, we can calculate inspirals as small corrections to the Newtonian results, and we indeed find that the eccentricity of a particle's orbit tends to become smaller as the particle spirals inwards. For very strong field orbits, however, it has been found that the reverse is true, and orbits become more eccentric with time [5]. There must, therefore be some radius (likely dependent on eccentricity and inclination) where the sign of \dot{e} passes through zero. As gravitational waves produced by a binary are expected to be strongly imprinted with the orbit's eccentricity, the location of this sign change is of interest for gravitational wave detection.

Chapter 2

The Mathematics of Inspirals

Though the general case of two gravitationally interacting bodies in GR is analytically intractable (albeit not numerically), the case where one particle is much lighter than the other can be analyzed through perturbation theory. In the case where the heavy object is a black hole, we have an analytic description (1.6) of the spacetime in the limit where the small object becomes a test mass, and we have an analytic description of the motion of such a test mass (1.9). The effects of the small object on the system can then be treated as a perturbation on this analytic solution.

2.1 The Teukolsky Formalism

For the case of a Kerr black hole, the perturbative expansion was carried out to first order in 1973 by Teukolsky [14]. Although the general metric perturbation involves ten real functions, it turns out that the part relevant to gravitational wave perturbations can be described by a single complex function ψ . Teukolsky derived a wave equation for ψ and showed that, somewhat amazingly, the equation was separable by writing

$$\psi = e^{-i\omega t} e^{im\varphi} S(\theta) R(r). \quad (2.1)$$

The function $S(\theta)$ is known as a spin-weighted spheroidal harmonic, and is a generalization of the familiar spherical harmonics. Spin-weighted spheroidal harmonics

can be evaluated numerically as described in Appendix A of [6]. The spin-weighted spheroidal harmonics are indexed by integers l and m just like spherical harmonics, except that we must have $l > |s|$, where s is known as the spin weight. For gravitational waves, $s = -2$.

The function $R(r)$, known as the radial Teukolsky function, obeys the differential equation

$$\Delta^{-s} \frac{d}{dr} \left(\Delta^{s+1} \frac{dR}{dr} \right) + V(r)R = \mathcal{T}(r) \quad (2.2)$$

with the Teukolsky potential given by

$$V(r) = \frac{K^2 - 2is(r - M)K}{\Delta} + 4is\omega r - \lambda \quad (2.3)$$

where $K = (r^2 + a^2)\omega - am$, λ is an eigenvalue associated with the spheroidal harmonic, Δ , a , and M , are as in (1.6), and \mathcal{T} is a source term dependent on the configuration of matter in the system. We are generally interested in inhomogeneous solutions to the Teukolsky equation, but these can be constructed from the homogeneous solution and the source term using Green's functions [2], so I will mostly focus on the case where \mathcal{T} is identically zero.

As a second order differential equation, (2.2) admits two independent solutions. A commonly chosen basis pair, due to their physical nature, is the “upgoing” solution, which has no waves coming in from infinity, and the “ingoing” solution, which has no waves emerging from the event horizon. These have asymptotic behavior [3]

$$R^{\text{in}}(r \rightarrow r_+) = B^{\text{trans}} \Delta^2 e^{-iPr^*} \quad (2.4)$$

$$R^{\text{in}}(r \rightarrow \infty) = B^{\text{ref}} r^3 e^{i\omega r^*} + B^{\text{inc}} r^{-1} e^{-i\omega r^*}$$

$$R^{\text{up}}(r \rightarrow r_+) = C^{\text{up}} e^{iPr^*} + C^{\text{ref}} \Delta^2 e^{-iPr^*} \quad (2.5)$$

$$R^{\text{up}}(r \rightarrow \infty) = C^{\text{trans}} r^3 e^{i\omega r^*}$$

where $P = \omega - ma/2Mr_+$ and r^* is the tortoise coordinate

$$r^* = r + \frac{2Mr_+}{r_+ - r_-} \log \frac{r - r_+}{2M} - \frac{2Mr_-}{r_+ - r_-} \log \frac{r - r_-}{2M}. \quad (2.6)$$

Note that the terms involving B^{inc} and C^{ref} are much smaller than the terms involving B^{ref} and C^{up} , so they will be difficult to extract from a numerical solution for $R(r)$. We will need B^{inc} for our calculations, so it is important to be able to extract the smaller components of these solutions accurately.

2.2 Evolution of “Constants” of Motion

As noted above, a particle orbiting a black hole will slowly radiate its energy away in gravitational waves and spiral into the hole. In the extreme mass ratio limit, the emitted waves are very weak, with amplitude proportional to the ratio of the small and large masses, μ/M . As usual for waves, the energy carried is proportional to the square of the amplitude, so, recalling that the (dimensionful) energy carried by the particle is proportional to its mass and using dimensional analysis, we find that $\dot{E} \sim (\mu/M^2)E$. As the orbital frequencies are independent of μ in this limit, we can see that the evolution is adiabatic for sufficiently small μ , that is, the time required for the energy to change significantly is large compared to the typical timescale of the orbit.

The inspiral can then be well approximated by a slow evolution between different orbits in the unperturbed Kerr spacetime. As each Kerr geodesic will be followed for a long time before the actual trajectory deviates from it significantly, we can average the wave emission over the orbit, thus eliminating any dependence on the various phases of the initial conditions, and leaving orbits described only by the conserved orbital parameters. We are also justified in Fourier transforming quantities dependent on the orbit without worrying about the effects of the inspiral changing our frequencies over the period integrated over in the transform.

On the longer timescales of the adiabatic evolution, the orbital parameters will no longer be conserved, so in order to calculate the details of the inspiral, we must find expressions for their rates of change. The most convenient orbital parametrization for this task is, perhaps not surprisingly, energy, angular momentum, and Carter constant.

2.2.1 Energy and Angular Momentum

Since the Kerr spacetime is asymptotically flat and energy and angular momentum are related to symmetries, we have global conservation laws for these quantities. This means we can calculate the change in our particle's energy and angular momentum as the negative of the amount radiated away in gravitational waves or absorbed by the hole.

The dominant contribution to the energy and angular momentum loss is from gravitational waves escaping to infinity. At large radius, the spacetime becomes flat and we can find the energy and momentum carried off by the waves using the Isaacson stress-energy tensor [7], which gives fluxes of

$$\frac{dp^\mu}{dA dt} = \frac{u^\mu}{16\pi} \left\langle \left(\frac{\partial h_+}{\partial t} \right)^2 + \left(\frac{\partial h_\times}{\partial t} \right)^2 \right\rangle \quad (2.7)$$

where u^μ is a vector pointing in the (lightlike) direction of propagation with $u^0 = 1$, h_+ and h_\times are the amplitudes of the plus and cross polarizations, and $\langle \cdot \rangle$ indicates an average over several wavelengths. At large radius, the Teukolsky function (2.1) becomes

$$\psi = \frac{\rho^{-4}}{2} (\ddot{h}_+ - i\ddot{h}_\times) \quad (2.8)$$

where $\rho = -1/(r - ia \cos \theta)$. Some manipulations with Green's functions performed in [2] then give the energy and angular momentum radiated to infinity in each mode of the field as

$$\dot{E}_{lmkn}^\infty = \frac{|Z_{lmkn}^H|^2}{4\pi\omega_{mkn}^2} \quad (2.9)$$

$$\dot{L}_{lmkn}^\infty = \frac{m}{\omega_{mkn}} \dot{E}_{lmkn}^\infty \quad (2.10)$$

where Z_{lmkn}^H is the prefactor of R^{up} in the inhomogeneous solution for large r , given by

$$Z_{lmkn}^H = -\frac{1}{2i\omega_{mkn} B_{lmkn}^{\text{inc}}} \int_{r_+}^{\infty} dr \frac{R_{lmkn}^{\text{up}} \mathcal{T}_{lmkn}}{\Delta^2} \quad (2.11)$$

and \mathcal{T}_{lmkn} is the source term in (2.2).

The energy and angular momentum absorbed by the hole can be calculated from the gravitational waves entering the event horizon. This is done in [15], which finds

$$\dot{E}_{lmkn}^H = \alpha_{lmkn} \frac{|Z_{lmkn}^\infty|^2}{4\pi\omega_{mkn}^2} \quad (2.12)$$

$$\dot{L}_{lmkn}^H = \frac{m}{\omega_{mkn}} \dot{E}_{lmkn}^\infty \quad (2.13)$$

where Z_{lmkn}^∞ is the prefactor of R^{in} in the inhomogeneous solution near the horizon, given by

$$Z_{lmkn}^\infty = -\frac{B_{lmkn}^{\text{trans}}}{2i\omega_{mkn} B_{lmkn}^{\text{inc}} C_{lmkn}^{\text{trans}}} \int_{r_+}^{\infty} dr \frac{R_{lmkn}^{\text{in}} \mathcal{T}_{lmkn}}{\Delta^2} \quad (2.14)$$

and α_{lmkn} is given in [6]. Note that for a point source on a bound orbit, \mathcal{T} only has support between r_{min} and r_{max} , so the integrals in (2.11) and (2.14) are over a finite range.

2.2.2 Carter Constant

The Carter constant is not related to a simple symmetry of the Kerr spacetime, so we cannot use simple conservation laws to calculate its change under radiation of gravitational waves. In special cases where the orbital evolution is constrained, the change in Carter constant can be determined from the evolution of the other parameters. For example, equatorial orbits must remain equatorial by symmetry, and also “circular” orbits (those with eccentricity $e = 0$) remain circular [8].

It has been common in the past when treating generic orbits (see, for example, [2]) to assume that the radiative evolution of orbits leaves the inclination angle unchanged. However, an argument leading to the general calculation of the Carter constant evolution was introduced in [10] and simplified in [12]¹. It was found that

$$\dot{Q}_{lmkn} = -2q^2 E \langle \cos^2 \theta \rangle \dot{E}_{lmkn} + 2L \langle \cot^2 \theta \rangle \dot{L}_{lmkn} - 2 \frac{k\Upsilon_\theta}{M^2\omega_{mkn}} \dot{E}_{lmkn} \quad (2.15)$$

where $\langle \cdot \rangle$ denotes averaging over the orbital path, and q is again a/M . It was also

¹Note that this reference refers to the value denoted here by Q as C and that there is a sign error in the second term of the last equation of the paper.

shown that this expression gives the correct results for equatorial and circular orbits.

Chapter 3

The MST Formalism and Fujita and Tagoshi's Method

To compute inspirals, then, the only remaining task is to solve the radial Teukolsky equation (2.2). However, the equation is not well suited to numerical integration because the potential $V(r)/\Delta$ is long range and because we need to extract the coefficients of subdominant solutions in (2.4) and (2.5). Previous work by my group (e.g., [6, 2]) avoided this problem using a method developed by Sasaki and Nakamura [13] relating the Teukolsky equation to another differential equation with a short range potential. This work uses a different, semianalytical, method developed by Fujita and Tagoshi [3, 4]¹, which writes the Teukolsky solutions directly as series of special functions.

3.1 The MST Formalism

Fujita and Tagoshi's method was developed from the formalism of Mano, Suzuki, and Takasugi (MST) [9]. This formalism expands each of the homogeneous solutions to the Teukolsky equation (2.2) as series of special functions in two different ways. For example, the ingoing solution can be written as a series of Gauss hypergeometric

¹This chapter is largely based on the two Fujita and Tagoshi papers cited here.

functions

$$R^{\text{in}} = e^{i\epsilon\kappa x} (-x)^{-s-i(\epsilon+\tau)/2} (1-x)^{i(\epsilon-\kappa)/2} \quad (3.1)$$

$$\times \sum_{n=-\infty}^{\infty} f_n^\nu {}_2F_1(n+\nu+1-i\tau, -n-\nu-i\tau; 1-s-i\epsilon-i\tau; x)$$

or as a series of confluent hypergeometric functions²

$$R^{\text{in}} = K_\nu R_C^\nu + K_{-\nu-1} R_C^{-\nu-1} \quad (3.2)$$

$$R_C^\nu = e^{-iz} 2^\nu z^{\nu-s} \left(1 - \frac{\epsilon\kappa}{z}\right)^{-s-i(\epsilon+\tau)/2} \frac{\Gamma(\nu+1-s+i\epsilon)}{\Gamma(2\nu+2)} \quad (3.3)$$

$$\times \sum_{n=-\infty}^{\infty} f_n^\nu (-2iz)^n \frac{(\nu+1+s-i\epsilon)_n}{(2\nu+2)_{2n}} {}_1F_1(n+\nu+1-s+i\epsilon; 2n+2\nu+2; 2iz)$$

where $\epsilon = 2M\omega$, $\kappa = \sqrt{1-q^2}$, $\tau = (\epsilon - mq)/\kappa$, $x = \omega(r_+ - r)/\epsilon\kappa$, $z = \omega(r - r_-)$, ${}_pF_q(\cdot)$ are hypergeometric functions, the K_ν are constants in r , f_n^ν is a sequence of coefficients which will be discussed later, and ν is the “renormalized angular momentum” which is adjusted to make the series converge. The first of these converges for all finite r , and the second converges for all points outside the horizon. There are similar expressions for R^{up} , the asymptotic amplitudes $B^{\text{inc,ref,trans}}$ and $C^{\text{ref,trans,up}}$, and the constants K_ν , but the expressions given here give a feel for the general form of MST quantities, so the others have been relegated to Appendix B.

Although we only need the value of the Teukolsky solutions in the physical region $r_+ < r < \infty$ where both series above converge, it is important to have both expressions for taking limits to find the asymptotic amplitudes (2.4) and (2.5). Also, when performing numerical calculations, the formally convergent series are sometimes found to have poor numerical behavior, with large terms canceling to give a small result. The regions where the sums are numerically well-behaved are generally different, so it is useful when calculating to have multiple methods available to obtain the same result.

²The subscript C stands for “Coulomb,” reflecting that the summands in the infinite sum and Coulomb wave functions (radial solutions to the quantum Hydrogen atom) are both written in terms of confluent hypergeometric functions.

3.2 Numerical MST

The MST formalism provides expressions for the Teukolsky solutions in terms of series, rather than integrals as in the Sasaki-Nakamura method, so it has the potential to be a powerful tool for numerical calculation. Before the series can be used, however, there are parameters that need to be determined. The expressions (3.1) and (3.3) contained the “renormalized angular momentum” ν and the series of coefficients f_n^ν , neither of which occurred in the original Teukolsky Equation (2.2), but which were introduced in the construction of the series solutions.

By substituting the series solutions into the differential equation, a recurrence relation between the coefficients f_n^ν can be derived. The relation is a simple three term recurrence

$$\alpha_n^\nu f_{n+1}^\nu + \beta_n^\nu f_n^\nu + \gamma_n^\nu f_{n-1}^\nu = 0 \quad (3.4)$$

with coefficients given by

$$\alpha_n^\nu = i\epsilon\kappa(n + \nu)(2n + 2\nu - 1) \left((n + \nu + 1 + s)^2 + \epsilon^2 \right) (n + \nu + 1 + i\tau) \quad (3.5)$$

$$\begin{aligned} \beta_n^\nu = & \left[(-\lambda - s(s + 1) + (n + \nu)(n + \nu + 1) + \epsilon^2 + \epsilon(\epsilon - mq)) (n + \nu)(n + \nu + 1) \right. \\ & \left. + \epsilon(\epsilon - mq) (s^2 + \epsilon^2) \right] (2n + 2\nu + 3)(2n + 2\nu - 1) \end{aligned} \quad (3.6)$$

$$\gamma_n^\nu = -i\epsilon\kappa(n + \nu + 1)(2n + 2\nu + 3) \left((n + \nu - s)^2 + \epsilon^2 \right) (n + \nu - i\tau). \quad (3.7)$$

Recall that λ is the eigenvalue of the spheroidal harmonic appearing in (2.3).

As a three term recurrence relation, (3.4) has two independent solutions. As n becomes large, the coefficients can either grow as

$$f_{n+1}^\nu \sim n f_n^\nu \quad (3.8)$$

or drop off as

$$f_{n+1}^\nu \sim n^{-1} f_n^\nu \quad (3.9)$$

and similarly for large negative n . It turns out that the f_n^ν dominate the large $|n|$ behavior of the series, so for the series to converge as $n \rightarrow \infty$ we must take the solution

(3.9), known as the minimal solution. Of course, the series must also converge for $n \rightarrow -\infty$, so we must take the minimal solution for negative n as well. However, we must have a single solution for all n , and the two minimal solutions do not generally coincide.

This is where the parameter ν comes in. We can vary the coefficients in (3.4) by varying ν and hopefully find a value where we have a single solution that is minimal for both large positive and negative n . To do this, let ${}^+f_n^\nu$ and ${}^-f_n^\nu$ be the solutions to the recurrence relation that are minimal for large positive and negative n , respectively, and let

$$R_n^\nu = \frac{{}^+f_n^\nu}{{}^+f_{n-1}^\nu} \quad L_n^\nu = \frac{{}^-f_n^\nu}{{}^-f_{n+1}^\nu} \quad (3.10)$$

be the ratios of adjacent terms for these solutions. Using (3.4), we can rewrite these as

$$R_n^\nu = -\frac{\gamma_n^\nu}{\beta_n^\nu + \alpha_n^\nu R_{n+1}^\nu} \quad L_n^\nu = -\frac{\alpha_n^\nu}{\beta_n^\nu + \gamma_n^\nu L_{n-1}^\nu}. \quad (3.11)$$

We can iterate this operation and construct continued fractions

$$R_n^\nu = -\frac{\gamma_n^\nu}{\beta_n^\nu - \frac{\alpha_n^\nu \gamma_{n+1}^\nu}{\beta_{n+1}^\nu - \frac{\alpha_{n+1}^\nu \gamma_{n+2}^\nu}{\beta_{n+2}^\nu - \dots}}} \quad L_n^\nu = -\frac{\alpha_n^\nu}{\beta_n^\nu - \frac{\gamma_n^\nu \alpha_{n-1}^\nu}{\beta_{n-1}^\nu - \frac{\gamma_{n-1}^\nu \alpha_{n-2}^\nu}{\beta_{n-2}^\nu - \dots}}} \quad (3.12)$$

which converge as the solutions ${}^+f_n^\nu$ and ${}^-f_n^\nu$ are minimal.

Our goal is to have ${}^+f_n^\nu = {}^-f_n^\nu$, which implies $R_n^\nu L_{n-1}^\nu = 1$. With a bit of further manipulation we find

$$\beta_n^\nu + \alpha_n^\nu R_{n+1}^\nu + \gamma_n^\nu R_{n-1}^\nu = 0. \quad (3.13)$$

This suggests that the ν matching the two minimal solutions can be identified by finding zeros of

$$g_n(\nu) = \beta_n^\nu + \alpha_n^\nu R_{n+1}^\nu + \gamma_n^\nu R_{n-1}^\nu. \quad (3.14)$$

The equation $g_n(\nu) = 0$ is referred to as the continued fraction equation. From the fact that both ${}^+f_n^\nu$ and ${}^-f_n^\nu$ satisfy the recurrence relation (3.4), it is clear that if $g_n(\nu) = 0$ is satisfied for one value of n , then it is satisfied for any n , so we will often

take $n = 0$. Once we have a ν satisfying $g_0(\nu) = 0$, we can use (3.10) to find the coefficients f_n^ν (up to an irrelevant overall normalization).

3.3 Solving the Continued Fraction Equation

It turns out that $g_0(\nu)$ has trivial zeros at all integer and half-integer ν except $\nu = -1/2$ which are not useful for constructing solutions. Additionally, it can easily be shown (see [4]) that if ν is a nontrivial zero of $g_n(\nu)$ then $\nu + k$ is as well for any integer k , that $g_0(\nu) = g_0(-\nu - 1)$, and that $g_0(x)$ and $g_0(-1/2 + ix)$ are both real for any real x . It also turns out that $g_n(\nu)$ always has a nontrivial zero, and that there are three possibilities for ν at this zero:

1. ν is real
2. ν has integer real part
3. ν has half-integer real part.

For small values of $|\omega|$, these cases can be distinguished by examining the value of $g_0(\nu)$ at $\nu = -1/2$ and its derivative at $\nu = 1$. As the continued fractions are poorly behaved at integers and half-integers, these values must be evaluated by (analytically) taking limits. The tests corresponding to the cases above are:

1. $g_0(-1/2) < 0$ and $g'_0(1)$ has the opposite sign than $\epsilon(\epsilon - mq)$
2. $g_0(-1/2) < 0$ and $g'_0(1)$ has the same sign as $\epsilon(\epsilon - mq)$
3. $g_0(-1/2) > 0$ and $g'_0(1)$ has the opposite sign than $\epsilon(\epsilon - mq)$.

Logically, there exists a fourth possibility [$g_0(-1/2) > 0$ and $g'_0(1)$ has the same sign as $\epsilon(\epsilon - mq)$], but it cannot occur.

For large values of $|\omega|$, we generally cannot evaluate these two special values well enough to determine their signs, and so are reduced to searching the three regions in sequence. It is generally found, however, that for large ω , the solution is almost always complex, with imaginary part increasing with increasing ω , as shown in Figure 3-1.

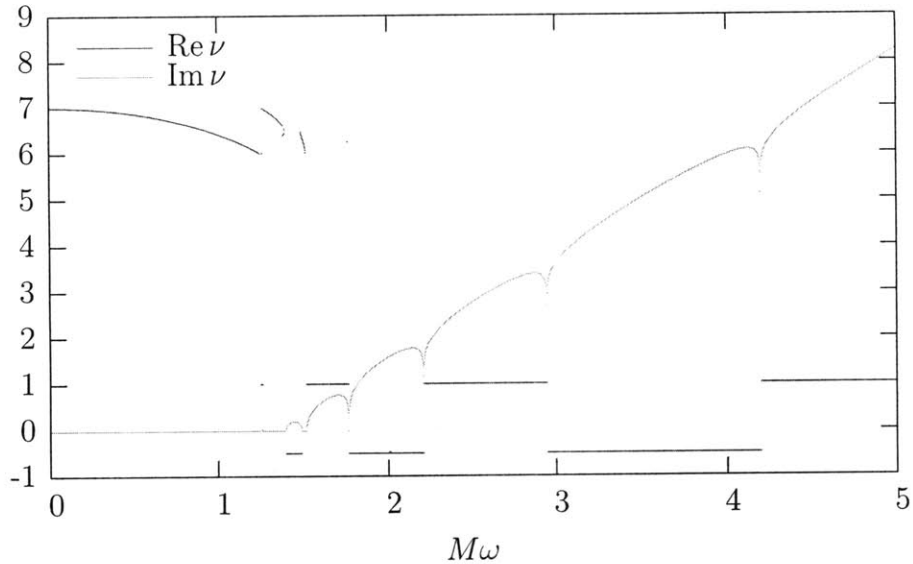


Figure 3-1: The value of ν that matches the minimal solutions for $l = m = 7, q = 0$ plotted against ω . Note that ν almost always has a large imaginary part for large ω . The jumps near $\omega = 1.4$ are the result of the code switching between different nontrivial roots of $g_0(\nu)$.

This is lucky, because while it becomes increasingly difficult to evaluate the function near the real line for large ω , the interesting values move out of that region.

While analytically any solution to the continued fraction equation would allow us to determine the expansion coefficients, particular solutions are often preferable numerically, either because they are easier to find or because they lead to numerically better behaved series. When searching for a root with half-integer real part, it is easiest to search the line $\nu = -1/2 + ix$, because, as noted above, the function values are all real there. I have found no particular reason to prefer different solutions with integer real parts, so have arbitrarily decided to search $\nu = 1 + ix$.

For real solutions, the process is more complicated. As noted above, if there is a real root, there are always an infinite number of them separated by integer steps, and also another infinite number obtained by reflecting the first set about $-1/2$. Analytically one would expect it to suffice to choose an integer and adjacent half-integer and search only the region between them. It is found numerically that most of these roots are very close to poles of $g_0(\nu)$, however, and thus not well suited to most root finding algorithms (see Figure 3-2). These poles also indicate that the

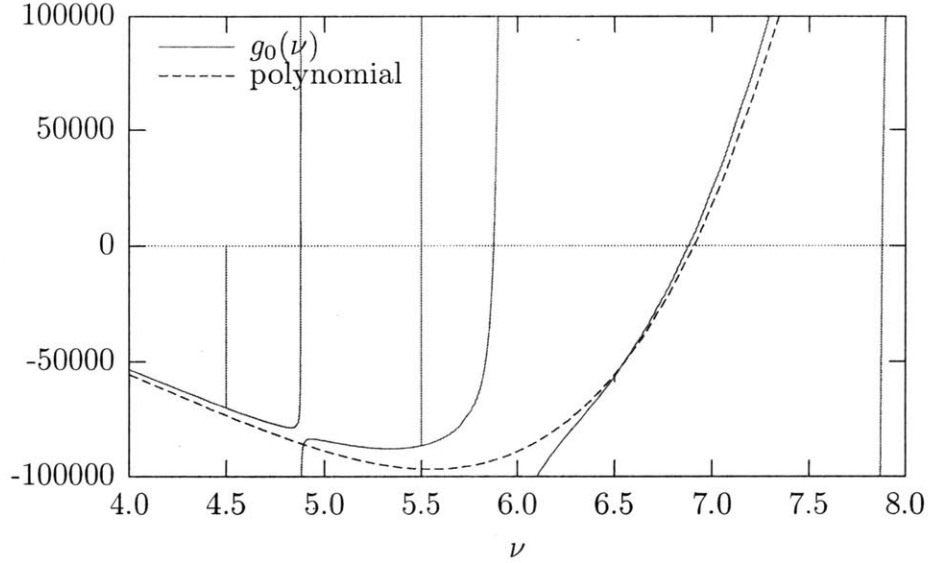


Figure 3-2: The function $g_0(\nu)$ for $l = m = 7$, $q = 0.99$, $M\omega = 0.5$ plotted for real ν , along with the polynomial approximation. The cleanest zero of $g_0(\nu)$ is at $\nu = 6.879$, while the polynomial zero is at $\nu = 6.906$. Note that the sharp features associated with the zeros at integer shifts of this. The zeros at points reflected in $\nu = -1/2$, as well as most of the trivial zeros, are near poles that are too sharp to be resolved on this plot.

series for R_n^ν and L_n^ν are poorly behaved in the region, so if these roots are used to evaluate the coefficients f_n^ν they will often lead to additional numerical errors.

By formally expanding the function for large $\nu + 1/2$, we find that, particularly at large ν , it is well approximated by a polynomial with an infinite number of poles added.³

$$\begin{aligned}
g_0(\nu)/4 &\approx (\nu + 1/2)^6 \\
&+ [-3/2 - \epsilon^2 \kappa^2 / 2 - (\lambda + s(s+1) - \epsilon^2 - \epsilon(\epsilon - mq))] (\nu + 1/2)^4 \\
&+ [9/16 + \epsilon \kappa \tau (\epsilon^2 + s^2) - \epsilon^2 \kappa^2 (\epsilon^2 - s^2 + 1/4) - \epsilon^2 \kappa^2 \tau^2 / 2 - \epsilon^4 \kappa^4 / 8 \\
&\quad + (5/4 - \epsilon^2 \kappa^2 / 2) (\lambda + s(s+1) - \epsilon^2 - \epsilon(\epsilon - mq))] (\nu + 1/2)^2 \\
&+ O(\nu + 1/2)^0.
\end{aligned} \tag{3.15}$$

³The next term in the expansion is roughly twice as long as all the preceding terms combined. I have not found it to be useful, as the effects of the poles are generally important in the region where such a term is significant, and adding another term would necessitate solving a cubic to find the approximate zero.

Although in the region we are interested in the poles often overlap and cause significant deviations from the polynomial form, the zero of the polynomial approximation is empirically found to provide a reasonable approximation to the most well behaved root of $g_0(\nu)$ in many situations, as in Figure 3-2. Even when the approximation becomes significantly worse, it is generally sufficient to search only a few half-integer regions near it.

Chapter 4

Implementation

Of course, in addition to generation of analytical formulas, any computational project is dependent on the implementation of these formulas in computer code. The main differences between analytical and numerical work in this case arise from the fact that the equations used in the MST formalism often involve infinite sums, which must be truncated at some point by a numerical algorithm. In addition, many of these sums turn out to have behavior which is problematic for numerical implementations.

4.1 Numerical Precision

In calculating the Teukolsky solution, two parts of the calculation were found to encapsulate most of the numerical inaccuracy. These were the calculation of the hypergeometric functions and the evaluation of the continued fractions (3.12).

The evaluation of the hypergeometric functions was found to be the most numerically problematic part of the code. The functions were evaluated by directly summing the hypergeometric series

$${}_pF_q(a_1, \dots, a_p; b_1, \dots, b_q; z) = \sum_{n=0}^{\infty} \frac{(a_1)_n \cdots (a_p)_n z^n}{(b_1)_n \cdots (b_q)_n n!}. \quad (4.1)$$

This series is often involves large terms canceling to give a very small result, and it was sometimes found to be necessary to use a multiple precision library to evaluate the

sum. This understandably causes a significant speed penalty in the code, however, so a version using extended precision (64 bit mantissa) floating point numbers was also implemented and the versions were chosen between at runtime based on the behavior of (4.1).

The continued fractions were less of a problem and only caused precision problems in a few cases. It was found that simply using extended precision code to sum the fractions was sufficient for the calculations I performed.

The other parts of the calculations were calculated using double precision floating point numbers, except for some of the internal variables used in summing the MST series (e.g., (3.1) and (3.3)), which were found to be susceptible to overflow. These were stored in extended precision, which provides 15 bit exponents, as opposed to the 11 bit exponents in double precision. The extra mantissa bits were not needed.

4.2 Algorithms and Truncation

Following Fujita and Tagoshi [3], I evaluated the continued fractions using Steed's algorithm [11]. When searching for roots of the continued fraction equation (3.14) on the real line or on the line $\text{Re } \nu = -1/2$, Brent's algorithm [11] was used. For $\text{Re } \nu = 1$, the function $g_0(\nu)$ was generally complex, so Brent's algorithm was not applicable and the secant method was used instead. The secant method was found to be more successful when applied to the function $\text{Im}(\nu)g_0(\nu)$ because this made the algorithm less likely to converge to the trivial zero at $\nu = 1$. The MST sums over the f_n^ν were truncated after 10 consecutive terms were below the required precision.

The code taking the Teukolsky solutions and producing fluxes is a descendant of the code used in [2], although heavily modified. The integrals involved in evaluating (2.11) and (2.14) (note that there is a second integral required to compute $\mathcal{T}(r)$) were evaluated using either the Clenshaw-Curtis method [11] or, when that was badly behaved, an adaptive Simpson method.

Once we have the fluxes for each mode, we must perform the sum over all the mode indices to obtain the changes in the orbital parameters. From symmetries of

the Teukolsky equation and related quantities, it can be shown that

$$Z_{l(-m)(-k)(-n)}^{H,\infty} = (-1)^{l+k} \bar{Z}_{lmkn}^{H,\infty} \quad (4.2)$$

where the bar represents complex conjugation. This means we only need to sum over half the harmonics and then double the result to get the total flux. I have chosen to break the sum as

$$\dot{E} = 2 \sum_{l=2}^{\infty} \sum_{m=0}^l \sum_{k=-\infty^*}^{\infty} \sum_{n=-\infty^*}^{\infty} \dot{E}_{lmkn} \quad (4.3)$$

where ∞^* indicates that the lower bound should be replaced by zero on the k sum if $m = 0$ and by one on the n sum if $m = k = 0$. The \dot{L} and \dot{Q} sums are done similarly.

Of course, the numerical implementation does not perform the infinite sums in full. It will be convenient for the following discussion to define \dot{E}_{lmk} to be the value of the innermost sum in (4.3), \dot{E}_{lm} to be the value of the innermost two sums, and \dot{E}_l to be the value of the inner three sums. Furthermore, define the symbol \dot{F} to indicate that a condition must hold for both \dot{E} and \dot{L} . To compute the fluxes to a requested accuracy ε , the l sum is started at $l = 2$ and summed over increasing l until

$$\dot{F}_l < \varepsilon \max_{\substack{l' \text{ already} \\ \text{computed}}} \dot{F}_{l'}.$$

For each l , the m sum is started at the value of m for which $\dot{E}_{(l-1)m}$ was largest in magnitude, and the sum proceeds in both directions until either the boundary of the sum is reached or

$$\dot{F}_{lm} < \varepsilon \max_{\substack{l'm' \text{ already} \\ \text{computed}}} \dot{F}_{l'm'}$$

and $\dot{F}_{lm} < \dot{F}_{lm_{\text{prev}}}$. The last condition ensures that the sum is not truncated when terms are increasing.

The starting values and truncation conditions involving ε for k and n are the obvious generalizations of those for m , but the requirements for terms to be decreasing are stricter. To truncate the k sum, I required three consecutive terms to be insignificant and decreasing.

The n sum was found to often have an oscillatory amplitude, so a strict requirement of decreasing values tended to cause many insignificant terms to be computed. The truncation condition on n was therefore expressed in terms of the maximum value on a moving window, so that isolated small harmonic fluxes would not prevent truncation. For truncation, it was required that either the maximum value in a moving window of length two was insignificant and decreasing for five summands or that the maximum in a window of length three was for eleven summands. Additionally, the last change was required to be a decrease.

Chapter 5

Results

Finally, in this chapter I present the numerical results of the calculations outlined above. I first present speed and accuracy comparisons with my group's Sasaki-Nakamura code and then accuracy comparisons with results from previous papers. Finally, I present new calculations showing the location of the $\dot{e} = 0$ surface for holes with spins $a = 0.2M$ and $a = 0.5M$.

5.1 Comparison with Sasaki-Nakamura

The implementation of Fujita and Tagoshi's numerical MST method (FT) was designed to replace our group's older method for evaluating the Teukolsky functions through the Sasaki-Nakamura transform (SN). It is important, therefore, to compare the performance of the two algorithms. The metrics considered here are the speed and accuracy of evaluation of the Teukolsky functions.

Both codes take a parameter controlling the accuracy of evaluation of the Teukolsky functions. This parameter has strong effects on the results of the SN code, so tests were run in that code at requested accuracies of 10^{-3} , 10^{-6} , and 10^{-9} . The parameter in the FT code is tunable at evaluation time and was not adjusted for these tests, resulting in all requests evaluating at the highest available precision. The evaluation time can sometimes be reduced in actual runs by adjusting this parameter to evaluate unimportant harmonics at lower accuracy.

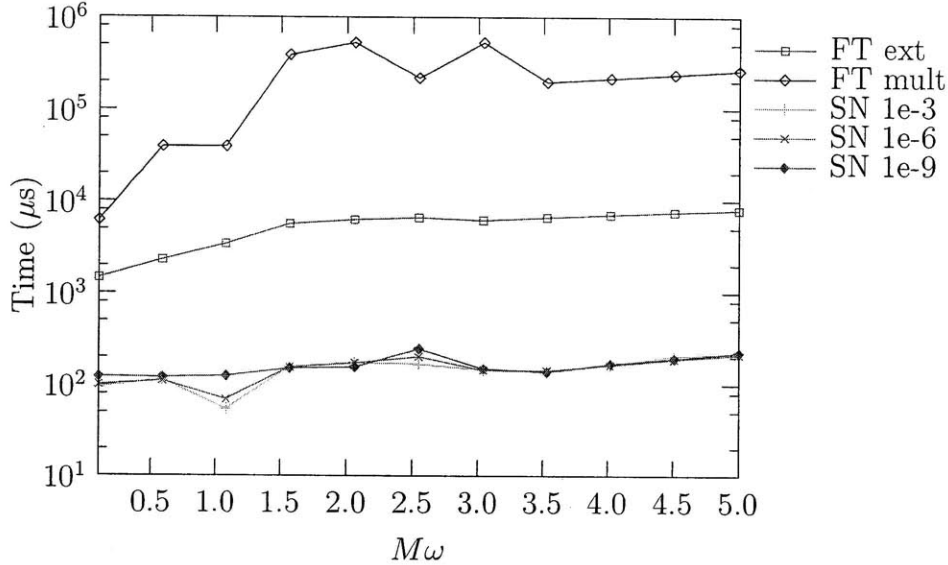


Figure 5-1: Evaluation times for the FT and SN solvers at $a = 0.5M$, $l = m = 6$, $p = 4.5M$, $e = 0.1$, $r = 4.5M$ for various ω . The evaluation times varied very little for different SN precision requests.

5.1.1 Speed Comparisons

Comparisons of the speeds of the algorithms are not as simple as one might hope. First of all, each method has an initialization procedure, which must be performed once per harmonic, and a procedure to evaluate the solutions at a particular radius, which may be evaluated many times per harmonic, particularly for eccentric orbits. Additionally, I often perform a calibration routine in the FT code to choose between different possible MST series. This calibration code can be omitted or shortened in controlled cases where a particular series is known to work well.

The evaluation of the Teukolsky solution was found to be much faster in the SN code than in the FT code (Figures 5-1 and 5-2). The initialization time when FT calibration was not performed showed the reverse relation with the FT code much faster than the SN code. The full FT calibration routine, however, involves many evaluations of the Teukolsky function and generally took as long or longer than the SN initialization (Figures 5-3 and 5-4).

As a result, the old SN code is faster in most cases. The exceptions are when only a few values of the Teukolsky solution are needed and the calibration procedure can

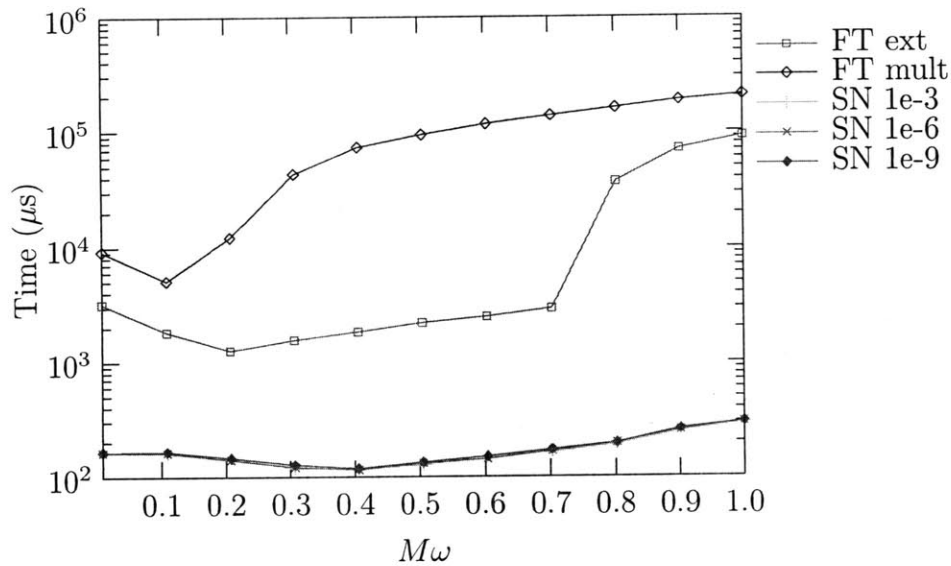


Figure 5-2: Evaluation times for the FT and SN solvers at $a = 0.2M$, $l = m = 6$, $p = 20M$, $e = 0.2$, $r = 20M$ for various ω . As in Figure 5-1, the SN evaluation time was nearly independent of precision.

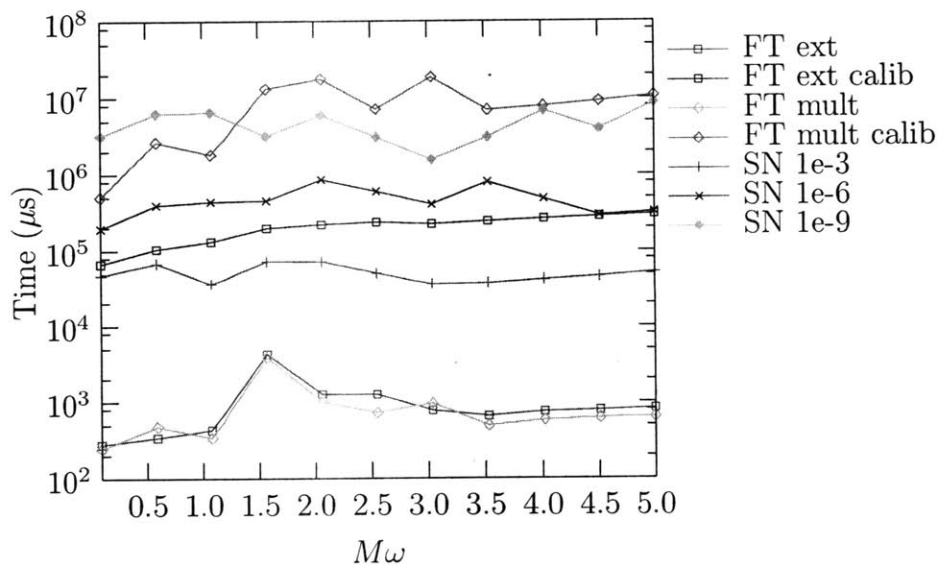


Figure 5-3: Initialization times for the FT and SN solvers at $a = 0.5M$, $l = m = 6$, $p = 4.5M$, $e = 0.1$, $r = 4.5M$ for various ω . Initialization times were virtually the same for the two FT runs because the multiple precision code is not used in the initialization procedure.

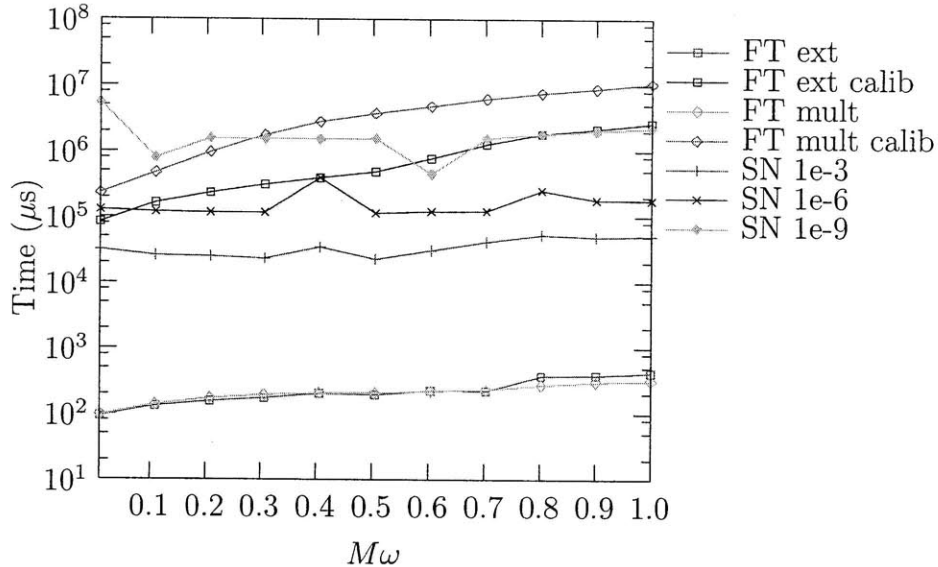


Figure 5-4: Initialization times for the FT and SN solvers at $a = 0.2M$, $l = m = 6$, $p = 20M$, $e = 0.2$, $r = 20M$ for various ω . As in Figure 5-3, multiple precision code was not used in the initialization of either FT run.

be shortened or eliminated. This often holds when considering circular orbits, as the calibration run time has dependence on eccentricity.

5.1.2 Precision Comparisons

The real advantage of the FT code, however, is in its precision capabilities. The FT solver attempts to evaluate the Teukolsky function to double precision, and, unless a lower precision is explicitly requested, the main source of error in the result is round-off error. Therefore, as an estimate of the accuracy of the FT code using multiple precision hypergeometric functions, I evaluated the function at 25 pairs of (r, ω) values in a grid spaced by (double precision) machine epsilon and recorded the largest deviation from the value in the grid center. This is a lower bound on the error in the evaluation, and is likely a good estimate. The other solvers' precisions were estimated from the larger of this noise estimate and their difference from the value given by the FT multiple precision evaluator.

In very strong field cases, such as the orbit with $p = 4.5M$ considered in Figure 5-5, there are significant round-off errors contributing from code outside the hypergeomet-

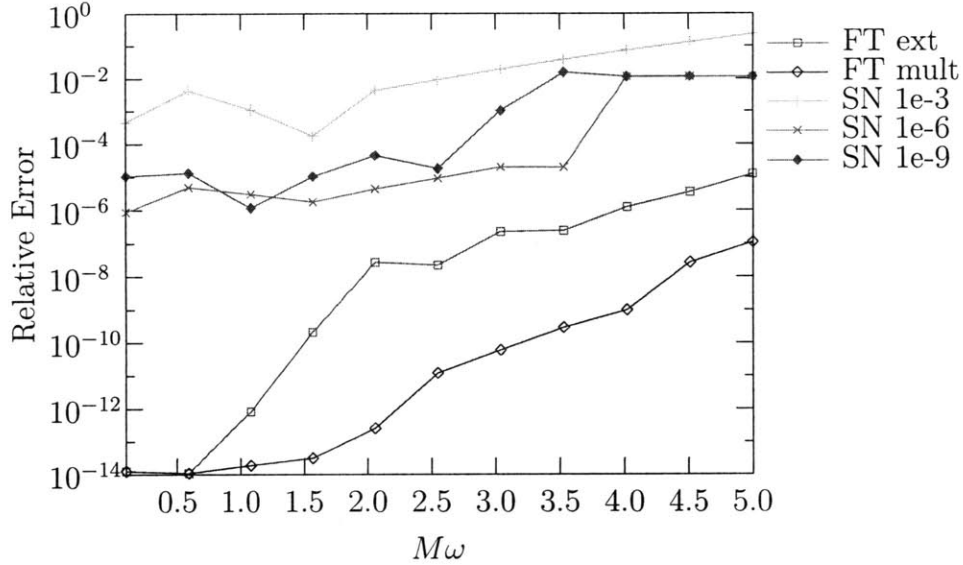


Figure 5-5: Relative error in the values of the Teukolsky solutions as evaluated by the FT and SN solvers at $a = 0.5M$, $l = m = 6$, $p = 4.5M$, $e = 0.1$, $r = 4.5M$ for various ω .

ric function evaluators. As a result, even the version of FT using multiple precision code was unable to maintain anything approaching double precision accuracy except for very small ω . However both versions of the FT solver were consistently much more accurate than any tested version of the SN solver, which by $M\omega = 5$ was only achieving accuracies of a part in 100.

In the weaker field case of $p = 20M$, shown in Figure 5-6, we can clearly see the difficulties in evaluating the hypergeometric function. The FT solver using multiple precision code for the hypergeometric function evaluator was able to maintain accuracies of 10^{-13} – 10^{-14} out to $M\omega = 1$, while the version using only extended precision was completely swamped by round-off error by $M\omega = 0.9$. The 10^{-6} SN solver also performed well and was consistently able to achieve accuracies of 10^{-5} – 10^{-6} throughout the range tested.

It is worth noting that the SN solver with requested precision of 10^{-9} did not generally achieve accuracy better than 10^{-6} , and in fact often was outperformed by the 10^{-6} SN solver despite having greatly increased initialization time. This suggests that, at least in the current implementation, the SN algorithm is unable to consistently achieve accuracies better than 10^{-6} .

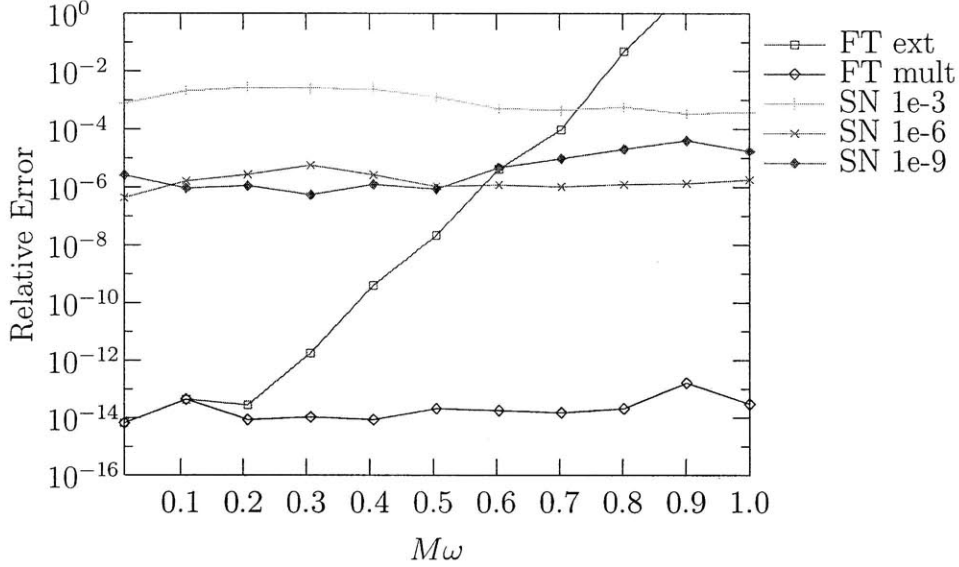


Figure 5-6: Relative error in the values of the Teukolsky solutions as evaluated by the FT and SN solvers at $a = 0.2M$, $l = m = 6$, $p = 20M$, $e = 0.2$, $r = 20M$ for various ω .

5.2 Comparison with Previous Results

I have compared fluxes for individual harmonics in high spin, strong field orbits with values given in Fujita and Tagoshi's papers [3, 4]. All my values were computed with a requested precision of 10^{-14} . For the values in Table 5.1, for circular equatorial orbits at $p = 3M$ around an $a = 0.998M$ hole, the computed energy fluxes differed by no more than a few parts in 10^{12} for any individual harmonic, and the differences were always less than 10^{-13} of the flux from the $l = m = 2$ harmonic. For the data in Table 5.2, which were chosen to have complex values of ν and are in an even stronger field ($a = 0.99M$, $p = 1.55M$) the agreement was not as good, with some harmonics differing by a few parts in 10^7 . As a fraction of the $l = m = 2$ flux, however, the values all agreed to almost 10^{-12} .

Tables 5.3–5.5 compare the total fluxes of energy and angular momentum to infinity and down the horizon with values reported by Glampedakis and Kennefick [5]. They estimate their error at no worse than 10^{-3} – 10^{-4} , and I generally confirm their results to 10^{-4} – 10^{-5} , with the notable exception of the down horizon fluxes for orbits around an $a = 0.5M$ hole, where we sometimes disagree by a few percent, and in one

l	$ m $	Fujita and Tagoshi [3]	This paper	Rel. error	Error/ E_{22}
2	1	$6.3283737145864869 \times 10^{-6}$	$6.3283737145863962 \times 10^{-6}$	1.43×10^{-14}	1.24×10^{-17}
2	2	$7.3350910900390372 \times 10^{-3}$	$7.3350910900386564 \times 10^{-3}$	5.19×10^{-14}	5.19×10^{-14}
3	1	$3.4517924227877552 \times 10^{-8}$	$3.4517924227877678 \times 10^{-8}$	3.83×10^{-15}	1.80×10^{-20}
3	2	$5.6458902861747337 \times 10^{-6}$	$5.6458902861747117 \times 10^{-6}$	3.90×10^{-15}	3.00×10^{-18}
3	3	$2.2084763695700243 \times 10^{-3}$	$2.2084763695701562 \times 10^{-3}$	5.97×10^{-14}	1.80×10^{-14}
4	1	$8.8426341846420484 \times 10^{-12}$	$8.8426341846419337 \times 10^{-12}$	1.30×10^{-14}	1.56×10^{-23}
4	2	$9.6507761069096606 \times 10^{-8}$	$9.6507761069096487 \times 10^{-8}$	1.23×10^{-15}	1.62×10^{-20}
4	3	$3.1572084515052529 \times 10^{-6}$	$3.1572084515053757 \times 10^{-6}$	3.89×10^{-14}	1.67×10^{-17}
4	4	$7.8979614897263311 \times 10^{-4}$	$7.8979614897259636 \times 10^{-4}$	4.65×10^{-14}	5.01×10^{-15}
5	1	$2.2266003587317006 \times 10^{-14}$	$2.2266003587316801 \times 10^{-14}$	9.21×10^{-15}	2.80×10^{-26}
5	2	$7.6236253541558626 \times 10^{-11}$	$7.6236253541560642 \times 10^{-11}$	2.64×10^{-14}	2.75×10^{-22}
5	3	$9.6377094209411545 \times 10^{-8}$	$9.6377094209402202 \times 10^{-8}$	9.70×10^{-14}	1.27×10^{-18}
5	4	$1.5240423964556889 \times 10^{-6}$	$1.5240423964556398 \times 10^{-6}$	3.22×10^{-14}	6.70×10^{-18}
5	5	$3.0439980326075501 \times 10^{-4}$	$3.0439980326075800 \times 10^{-4}$	9.97×10^{-15}	4.14×10^{-16}
6	1	$3.8509863211419323 \times 10^{-18}$	$3.8509863211420001 \times 10^{-18}$	1.76×10^{-14}	9.24×10^{-30}
6	2	$5.7360410503468190 \times 10^{-13}$	$5.7360410503468705 \times 10^{-13}$	8.98×10^{-15}	7.02×10^{-25}
6	3	$1.3155762424734953 \times 10^{-10}$	$1.3155762424734402 \times 10^{-10}$	4.19×10^{-14}	7.51×10^{-22}
6	4	$6.7884404091806854 \times 10^{-8}$	$6.7884404091798980 \times 10^{-8}$	1.16×10^{-13}	1.07×10^{-18}
6	5	$6.9003809076206216 \times 10^{-7}$	$6.9003809076206555 \times 10^{-7}$	4.91×10^{-15}	4.62×10^{-19}
6	6	$1.2192534271212692 \times 10^{-4}$	$1.2192534271233083 \times 10^{-4}$	1.67×10^{-12}	2.78×10^{-14}
7	1	$5.0631852897823082 \times 10^{-21}$	$5.0631852897825580 \times 10^{-21}$	4.93×10^{-14}	3.41×10^{-32}
7	2	$3.1060171837611518 \times 10^{-16}$	$3.1060171837611498 \times 10^{-16}$	6.35×10^{-16}	2.69×10^{-29}
7	3	$1.7698525192439268 \times 10^{-12}$	$1.7698525192441090 \times 10^{-12}$	1.03×10^{-13}	2.48×10^{-23}
7	4	$1.2846205001945888 \times 10^{-10}$	$1.2846205001946045 \times 10^{-10}$	1.23×10^{-14}	2.15×10^{-22}
7	5	$4.0511763345368075 \times 10^{-8}$	$4.0511763345352921 \times 10^{-8}$	3.74×10^{-13}	2.07×10^{-18}
7	6	$3.0238471412501713 \times 10^{-7}$	$3.0238471412511279 \times 10^{-7}$	3.16×10^{-13}	1.30×10^{-17}
7	7	$4.9939392339609413 \times 10^{-5}$	$4.9939392339549003 \times 10^{-5}$	1.21×10^{-12}	8.24×10^{-15}

Table 5.1: Energy fluxes (scaled by M^2/μ) to infinity for circular equatorial orbits at $p = 3M$ around an $a = 0.998M$ hole compared to the values in Fujita and Tagoshi [3]. The magnitude of the relative error between the values and the error divided by the flux from the largest harmonic are also given. Values were computed with a requested tolerance of 10^{-14} .

l	$ m $	Fujita and Tagoshi [4]	This paper	Rel. error	Error/ E_{22}
2	2	$3.568033154338851 \times 10^{-2}$	$3.568033154338834 \times 10^{-2}$	4.86×10^{-15}	4.86×10^{-15}
3	3	$2.152959342790158 \times 10^{-2}$	$2.152959342790170 \times 10^{-2}$	5.48×10^{-15}	3.31×10^{-15}
4	4	$1.230541952573211 \times 10^{-2}$	$1.230541952573288 \times 10^{-2}$	6.25×10^{-14}	2.15×10^{-14}
5	4	$1.933924400940079 \times 10^{-5}$	$1.933924400868041 \times 10^{-5}$	3.72×10^{-11}	2.02×10^{-14}
5	5	$7.259849874157195 \times 10^{-3}$	$7.259849874157374 \times 10^{-3}$	2.46×10^{-14}	5.01×10^{-15}
6	5	$1.536520289551414 \times 10^{-5}$	$1.536520289374150 \times 10^{-5}$	1.15×10^{-10}	4.97×10^{-14}
6	6	$4.404599359654937 \times 10^{-3}$	$4.404599359655978 \times 10^{-3}$	2.36×10^{-13}	2.92×10^{-14}
7	6	$1.148795883734041 \times 10^{-5}$	$1.148795883372663 \times 10^{-5}$	3.15×10^{-10}	1.01×10^{-13}
7	7	$2.726949666682515 \times 10^{-3}$	$2.726949666686628 \times 10^{-3}$	1.51×10^{-12}	1.15×10^{-13}
8	7	$8.267168128593364 \times 10^{-6}$	$8.267168127097673 \times 10^{-6}$	1.81×10^{-10}	4.19×10^{-14}
8	8	$1.713110726903289 \times 10^{-3}$	$1.713110726887038 \times 10^{-3}$	9.49×10^{-12}	4.55×10^{-13}
9	7	$1.650193971262395 \times 10^{-7}$	$1.650193658201491 \times 10^{-7}$	1.90×10^{-7}	8.77×10^{-13}
9	8	$5.800152000099428 \times 10^{-6}$	$5.800151998295866 \times 10^{-6}$	3.11×10^{-10}	5.05×10^{-14}
9	9	$1.087830324625970 \times 10^{-3}$	$1.087830324591859 \times 10^{-3}$	3.14×10^{-11}	9.56×10^{-13}
10	8	$1.423939557356283 \times 10^{-7}$	$1.423939936276081 \times 10^{-7}$	2.66×10^{-7}	1.06×10^{-12}
10	9	$3.998328388790399 \times 10^{-6}$	$3.998328381658750 \times 10^{-6}$	1.78×10^{-9}	2.00×10^{-13}
10	10	$6.963929698290593 \times 10^{-4}$	$6.963929698438952 \times 10^{-4}$	2.13×10^{-11}	4.16×10^{-13}

Table 5.2: Energy fluxes (scaled by M^2/μ) to infinity for circular equatorial orbits at $p = 1.55M$ around an $a = 0.99M$ hole compared to the values in Fujita and Tagoshi [4], which were chosen so that ν was complex with half integer real part. Values were computed with a requested tolerance of 10^{-14} .

case ($e = 0.4$, $p = 4.90M$) by nearly 10%.

Tables 5.6 and 5.7 compare total fluxes to infinity and down horizon for generic orbits with those from Drasco and Hughes [2]. Their fluxes are estimated to be accurate to 10^{-3} – 10^{-4} and I generally confirm their values to that accuracy or better. In contrast with the comparison with Glampedakis and Kennefick, agreement is particularly good on down horizon fluxes.

5.3 The $\dot{e} = 0$ Surface

As mentioned in Section 1.4, there must be some surface in the (p, e, θ_{\min}) space of orbits which divides the Newtonian-like circularizing evolution, where $\dot{e} < 0$ from the strong field evolution where $\dot{e} > 0$. With an algorithm able to evaluate the Teukolsky solutions to high accuracy even in strong field regions, we are now prepared to compute the location of this surface. Glampedakis and Kennefick used a solver based on the Sasaki-Nakamura transform to locate the $\dot{e} = 0$ curve for equatorial orbits [5]. I have confirmed their result for $a = 0.5M$ orbits in Figure 5-7 with a

e	p/M	$(M^2/\mu)\dot{E}^\infty$	$(M^2/\mu)\dot{E}^H$	$(M^2/\mu)\dot{L}^\infty$	$(M^2/\mu)\dot{L}^H$
0.10	4.60	$2.88029911 \times 10^{-3}$	$-6.40925149 \times 10^{-6}$	$2.88686886 \times 10^{-2}$	$-6.47037374 \times 10^{-5}$
		2.88029 $\times 10^{-3}$	-6.41673 $\times 10^{-6}$	2.88686 $\times 10^{-2}$	-6.47058 $\times 10^{-5}$
0.10	5.00	$1.81736240 \times 10^{-3}$	$-4.02415542 \times 10^{-6}$	$2.06724594 \times 10^{-2}$	$-4.58625239 \times 10^{-5}$
		1.81736 $\times 10^{-3}$	-4.03021 $\times 10^{-6}$	2.06724 $\times 10^{-2}$	-4.58643 $\times 10^{-5}$
0.10	6.00	$7.10653140 \times 10^{-4}$	$-1.27378969 \times 10^{-6}$	$1.05537107 \times 10^{-2}$	$-1.88238940 \times 10^{-5}$
		7.10665 $\times 10^{-4}$	-1.27547 $\times 10^{-6}$	1.05539 $\times 10^{-2}$	-1.88243 $\times 10^{-5}$
0.20	4.70	$3.11811419 \times 10^{-3}$	$-5.68844881 \times 10^{-6}$	$2.96691981 \times 10^{-2}$	$-5.63722245 \times 10^{-5}$
		3.11812 $\times 10^{-3}$	-5.71886 $\times 10^{-6}$	2.96692 $\times 10^{-2}$	-5.63759 $\times 10^{-5}$
0.20	5.00	$2.09140784 \times 10^{-3}$	$-4.24513094 \times 10^{-6}$	$2.21226787 \times 10^{-2}$	$-4.58864578 \times 10^{-5}$
		2.09142 $\times 10^{-3}$	-4.27185 $\times 10^{-6}$	2.21228 $\times 10^{-2}$	-4.58884 $\times 10^{-5}$
0.20	6.00	$7.78552936 \times 10^{-4}$	$-1.42994405 \times 10^{-6}$	$1.08488123 \times 10^{-2}$	$-1.97301294 \times 10^{-5}$
		7.78541 $\times 10^{-4}$	-1.43776 $\times 10^{-6}$	1.08487 $\times 10^{-2}$	-1.97306 $\times 10^{-5}$
0.30	4.70	$4.96252291 \times 10^{-3}$	$-2.29914952 \times 10^{-6}$	$4.07606137 \times 10^{-2}$	$-2.63157686 \times 10^{-5}$
		4.96241 $\times 10^{-3}$	-2.34257 $\times 10^{-6}$	4.07599 $\times 10^{-2}$	-2.62670 $\times 10^{-5}$
0.30	5.00	$2.60438719 \times 10^{-3}$	$-3.72945859 \times 10^{-6}$	$2.48383086 \times 10^{-2}$	$-3.98838822 \times 10^{-5}$
		2.60439 $\times 10^{-3}$	-3.79849 $\times 10^{-6}$	2.48384 $\times 10^{-2}$	-3.98856 $\times 10^{-5}$
0.30	6.00	$8.88287360 \times 10^{-4}$	$-1.61038937 \times 10^{-6}$	$1.12980424 \times 10^{-2}$	$-2.06377084 \times 10^{-5}$
		8.88282 $\times 10^{-4}$	-1.63235 $\times 10^{-6}$	1.12981 $\times 10^{-2}$	-2.06383 $\times 10^{-5}$
0.40	4.90	$4.52498150 \times 10^{-3}$	$2.83703121 \times 10^{-6}$	$3.62876348 \times 10^{-2}$	$8.76348623 \times 10^{-6}$
		4.52598 $\times 10^{-3}$	+3.00302 $\times 10^{-6}$	3.62936 $\times 10^{-2}$	+9.69843 $\times 10^{-6}$
0.40	6.00	$1.03262466 \times 10^{-3}$	$-1.63468538 \times 10^{-6}$	$1.18255840 \times 10^{-2}$	$-2.03394199 \times 10^{-5}$
		1.03261 $\times 10^{-3}$	-1.68472 $\times 10^{-6}$	1.18257 $\times 10^{-2}$	-2.03399 $\times 10^{-5}$

Table 5.3: Comparison with numerical results by Glampedakis and Kennefick for eccentric prograde equatorial orbits around a spin $a = 0.5M$ hole. The first line of each pair is my data calculated with a requested precision of 10^{-8} , and the second line is the value reported in [5].

e	p/M	$(M^2/\mu)\dot{E}^\infty$	$(M^2/\mu)\dot{E}^H$	$(M^2/\mu)\dot{L}^\infty$	$(M^2/\mu)\dot{L}^H$
0.10	1.55	$9.28403015 \times 10^{-2}$	$-7.84631276 \times 10^{-3}$	$2.64042554 \times 10^{-1}$	$-2.22987881 \times 10^{-2}$
		9.26325 $\times 10^{-2}$	-7.85155 $\times 10^{-3}$	2.63428 $\times 10^{-1}$	-2.23134 $\times 10^{-2}$
0.10	2.00	$4.72368202 \times 10^{-2}$	$-3.16311295 \times 10^{-3}$	$1.77547292 \times 10^{-1}$	$-1.18563028 \times 10^{-2}$
		4.72325 $\times 10^{-2}$	-3.16550 $\times 10^{-3}$	1.77532 $\times 10^{-1}$	-1.18650 $\times 10^{-2}$
0.10	3.00	$1.12399333 \times 10^{-2}$	$-4.14238366 \times 10^{-4}$	$6.83341074 \times 10^{-2}$	$-2.50310835 \times 10^{-3}$
		1.12400 $\times 10^{-2}$	-4.14404 $\times 10^{-4}$	6.83347 $\times 10^{-2}$	-2.50408 $\times 10^{-3}$
0.20	3.00	$1.19894749 \times 10^{-2}$	$-4.59150587 \times 10^{-4}$	$6.94435790 \times 10^{-2}$	$-2.60622702 \times 10^{-3}$
		1.19893 $\times 10^{-2}$	-4.59376 $\times 10^{-4}$	6.94427 $\times 10^{-2}$	-2.60733 $\times 10^{-3}$

Table 5.4: Same as Table 5.3, except for a spin $a = 0.99M$ hole.

e	p/M	$(M^2/\mu)\dot{E}^\infty$	$(M^2/\mu)\dot{E}^H$	$(M^2/\mu)\dot{L}^\infty$	$(M^2/\mu)\dot{L}^H$
0.10	9.5	$1.22525287 \times 10^{-4}$	$1.50993569 \times 10^{-6}$	$-3.31416271 \times 10^{-3}$	$-3.98342328 \times 10^{-5}$
		1.22528×10^{-4}	1.50991×10^{-6}	-3.31424×10^{-3}	-3.98335×10^{-5}
0.10	11.0	$4.99493099 \times 10^{-5}$	$3.39591366 \times 10^{-7}$	$-1.72493157 \times 10^{-3}$	$-1.13847429 \times 10^{-5}$
		4.99506×10^{-5}	3.39590×10^{-7}	-1.72497×10^{-3}	-1.13847×10^{-5}
0.20	9.7	$1.40483464 \times 10^{-4}$	$2.21416564 \times 10^{-6}$	$-3.53938931 \times 10^{-3}$	$-5.25892620 \times 10^{-5}$
		1.40484×10^{-4}	2.21408×10^{-6}	-3.53943×10^{-3}	-5.25871×10^{-5}
0.20	11.0	$5.63934277 \times 10^{-5}$	$5.01281136 \times 10^{-7}$	$-1.80665235 \times 10^{-3}$	$-1.47518536 \times 10^{-5}$
		5.63927×10^{-5}	5.01279×10^{-7}	-1.80663×10^{-3}	-1.47518×10^{-5}
0.30	10.0	$1.49711929 \times 10^{-4}$	$2.90977239 \times 10^{-6}$	$-3.53876006 \times 10^{-3}$	$-6.33610134 \times 10^{-5}$
		1.49711×10^{-4}	2.90957×10^{-6}	-3.53885×10^{-3}	-6.33565×10^{-5}
0.30	11.0	$6.74023322 \times 10^{-5}$	$8.29944762 \times 10^{-7}$	$-1.94161860 \times 10^{-3}$	$-2.11329488 \times 10^{-5}$
		6.74024×10^{-5}	8.29938×10^{-7}	-1.94163×10^{-3}	-2.11328×10^{-5}
0.40	10.3	$1.57139435 \times 10^{-4}$	$3.72830877 \times 10^{-6}$	$-3.47122771 \times 10^{-3}$	$-7.49463504 \times 10^{-5}$
		1.57135×10^{-4}	3.72816×10^{-6}	-3.47105×10^{-3}	-7.49426×10^{-5}
0.40	11.0	$8.33669911 \times 10^{-5}$	$1.42913822 \times 10^{-6}$	$-2.12769757 \times 10^{-3}$	$-3.18081101 \times 10^{-5}$
		8.33663×10^{-5}	1.42912×10^{-6}	-2.12770×10^{-3}	-3.18078×10^{-5}
0.50	10.4	$2.46733224 \times 10^{-4}$	$8.15263449 \times 10^{-6}$	$-4.73608348 \times 10^{-3}$	$-1.46441206 \times 10^{-4}$
		2.46763×10^{-4}	8.15567×10^{-6}	-4.73640×10^{-3}	-1.46459×10^{-4}
0.50	11.0	$1.04909170 \times 10^{-4}$	$2.47886538 \times 10^{-6}$	$-2.36298876 \times 10^{-3}$	$-4.88980710 \times 10^{-5}$
		1.04907×10^{-4}	2.47885×10^{-6}	-2.36298×10^{-3}	-4.88973×10^{-5}

Table 5.5: Same as Table 5.3, except for retrograde orbits around a spin $a = 0.99M$ hole.

e	θ_{\min}	$(M^2/\mu)\dot{E}^\infty$	$(M^2/\mu)\dot{E}^H$	$(M^2/\mu)\dot{L}^\infty$	$(M^2/\mu)\dot{L}^H$
0.1	70°	$5.87406088 \times 10^{-4}$	$-4.25755582 \times 10^{-6}$	$8.53661432 \times 10^{-3}$	$-6.72409718 \times 10^{-5}$
		5.87399×10^{-4}	-4.25756×10^{-6}	8.53652×10^{-3}	-6.72410×10^{-5}
0.1	50°	$6.18509450 \times 10^{-4}$	$-3.96691978 \times 10^{-6}$	$7.62833651 \times 10^{-3}$	$-7.76672985 \times 10^{-5}$
		6.18500×10^{-4}	-3.96692×10^{-6}	7.62823×10^{-3}	-7.76672×10^{-5}
0.1	30°	$6.83866668 \times 10^{-4}$	$-3.36170687 \times 10^{-6}$	$6.07274919 \times 10^{-3}$	$-1.12143506 \times 10^{-4}$
		6.83855×10^{-4}	-3.36171×10^{-6}	6.07264×10^{-3}	-1.12143×10^{-4}
0.1	10°	$8.06828209 \times 10^{-4}$	$-9.78644624 \times 10^{-7}$	$3.61885454 \times 10^{-3}$	$-1.90843400 \times 10^{-4}$
		8.07007×10^{-4}	-9.78653×10^{-7}	3.61820×10^{-3}	-1.90843×10^{-4}
0.3	70°	$6.80445754 \times 10^{-4}$	$-5.88185745 \times 10^{-6}$	$8.62450122 \times 10^{-3}$	$-7.78419472 \times 10^{-5}$
		6.80432×10^{-4}	-5.88185×10^{-6}	8.62437×10^{-3}	-7.78419×10^{-5}
0.3	50°	$7.26803050 \times 10^{-4}$	$-5.88820547 \times 10^{-6}$	$7.83518320 \times 10^{-3}$	$-1.00627987 \times 10^{-4}$
		7.26781×10^{-4}	-5.88820×10^{-6}	7.83499×10^{-3}	-1.00628×10^{-4}
0.3	30°	$8.31592110 \times 10^{-4}$	$-5.28977216 \times 10^{-6}$	$6.48735187 \times 10^{-3}$	$-1.66905340 \times 10^{-4}$
		8.31504×10^{-4}	-5.28978×10^{-6}	6.48662×10^{-3}	-1.66905×10^{-4}
0.3	10°	$1.08618818 \times 10^{-3}$	$-1.52552341 \times 10^{-7}$	$4.37169436 \times 10^{-3}$	$-3.46175307 \times 10^{-4}$
		1.08629×10^{-3}	-1.52779×10^{-7}	4.36910×10^{-3}	-3.46171×10^{-4}

Table 5.6: Comparison with numerical results by Drasco and Hughes for inclined, eccentric prograde orbits around a spin $a = 0.9M$ hole with $p = 6M$. The first line of each pair is my data calculated with a requested precision of 10^{-8} , and the second line is the value reported in [2].

e	θ_{\min}	$(M^2/\mu)\dot{E}^\infty$	$(M^2/\mu)\dot{E}^H$	$(M^2/\mu)\dot{L}^\infty$	$(M^2/\mu)\dot{L}^H$
0.1	-10°	$2.51101673 \times 10^{-5}$	$1.10408309 \times 10^{-8}$	$-1.22380591 \times 10^{-4}$	$-1.85761038 \times 10^{-6}$
		2.50845×10^{-5}	-1.10409×10^{-8}	-1.22779×10^{-4}	-1.85760×10^{-6}
0.1	-30°	$2.67635055 \times 10^{-5}$	$3.80215497 \times 10^{-8}$	$-4.91743299 \times 10^{-4}$	$-2.47773849 \times 10^{-6}$
		2.67639×10^{-5}	3.80216×10^{-8}	-4.91749×10^{-4}	-2.47774×10^{-6}
0.1	-50°	$2.83941424 \times 10^{-5}$	$7.36703876 \times 10^{-8}$	$-8.40630757 \times 10^{-4}$	$-3.36034200 \times 10^{-6}$
		2.83939×10^{-5}	7.36704×10^{-8}	-8.40626×10^{-4}	-3.36034×10^{-6}
0.1	-70°	$2.96243014 \times 10^{-5}$	$1.06499809 \times 10^{-7}$	$-1.09778053 \times 10^{-3}$	$-4.23915116 \times 10^{-6}$
		2.96240×10^{-5}	1.06500×10^{-7}	-1.09777×10^{-3}	-4.23915×10^{-6}
0.3	-10°	$2.92463760 \times 10^{-5}$	$2.44837650 \times 10^{-8}$	$-1.14149035 \times 10^{-4}$	$-2.74782369 \times 10^{-6}$
		2.92408×10^{-5}	2.44837×10^{-8}	-1.14269×10^{-4}	-2.74782×10^{-6}
0.3	-30°	$3.18177793 \times 10^{-5}$	$7.99023301 \times 10^{-8}$	$-4.92331397 \times 10^{-4}$	$-3.86655915 \times 10^{-6}$
		3.18207×10^{-5}	7.99022×10^{-8}	-4.92316×10^{-4}	-3.86655×10^{-6}
0.3	-50°	$3.45505039 \times 10^{-5}$	$1.57246246 \times 10^{-7}$	$-8.65362467 \times 10^{-4}$	$-5.43045357 \times 10^{-6}$
		3.45503×10^{-5}	1.57246×10^{-7}	-8.65358×10^{-4}	-5.43045×10^{-6}
0.3	-70°	$3.67888755 \times 10^{-5}$	$2.32108725 \times 10^{-7}$	$-1.15339840 \times 10^{-3}$	$-6.98894974 \times 10^{-6}$
		3.67886×10^{-5}	2.32108×10^{-7}	-1.15339×10^{-3}	-6.98894×10^{-6}
0.5	-10°	$3.44246391 \times 10^{-5}$	$6.01946990 \times 10^{-8}$	$-9.51575958 \times 10^{-5}$	$-4.38713536 \times 10^{-6}$
		3.44049×10^{-5}	6.01938×10^{-8}	-9.51540×10^{-5}	-4.38711×10^{-6}
0.5	-30°	$3.87670910 \times 10^{-5}$	$1.87176401 \times 10^{-7}$	$-4.68896315 \times 10^{-4}$	$-6.64498626 \times 10^{-6}$
		3.87672×10^{-5}	1.87174×10^{-7}	-4.68684×10^{-4}	-6.64495×10^{-6}
0.5	-50°	$4.37797072 \times 10^{-5}$	$3.77540991 \times 10^{-7}$	$-8.67407548 \times 10^{-4}$	$-9.86403051 \times 10^{-6}$
		4.37778×10^{-5}	3.77537×10^{-7}	-8.67384×10^{-4}	-9.86398×10^{-6}
0.5	-70°	$4.82955053 \times 10^{-5}$	$5.75311579 \times 10^{-7}$	$-1.20171197 \times 10^{-3}$	$-1.31850289 \times 10^{-5}$
		4.82937×10^{-5}	5.75306×10^{-7}	-1.20168×10^{-3}	-1.31850×10^{-5}

Table 5.7: Same as Table 5.6, but for retrograde orbits with $p = 12M$.

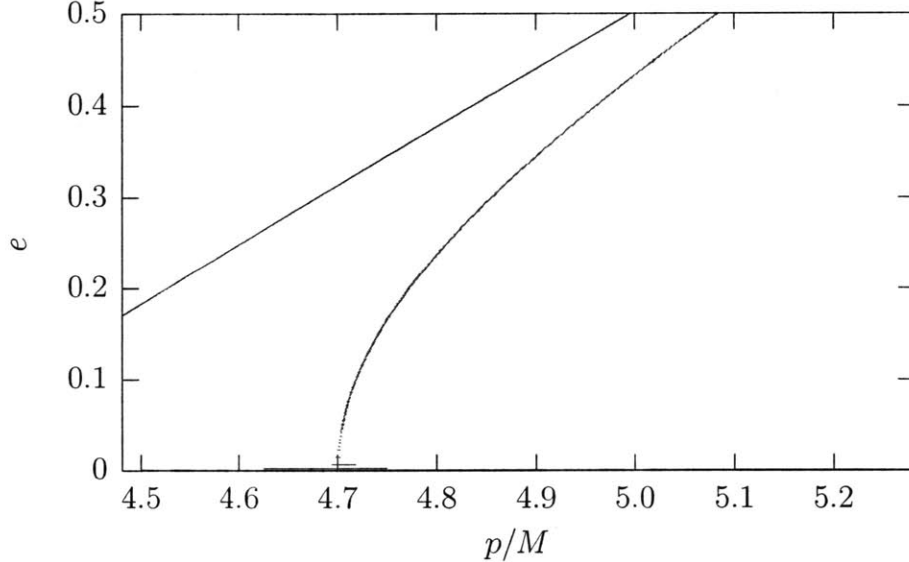


Figure 5-7: The $\dot{e} = 0$ curve for prograde equatorial orbits around a spin $a = 0.5M$ hole, as well as the location of the innermost stable orbits: Compare the upper right image in FIG. 5 of [5]. Points were computed with a maximum precision of 10^{-6} . Note that each point has a horizontal error bar, which is only visible for the nearly circular orbits.

much finer grid of points. I have not yet attempted to duplicate their results for higher spin holes.

Additionally, using the prescription from [10], I have found the $\dot{e} = 0$ curves for θ_{\min} inclinations spaced at 15° intervals (excluding $\theta_{\min} = 0$, which passes through a coordinate singularity at the pole of the spherical coordinate system) for central holes of spins $a = 0.2M$ (Figure 5-8) and $a = 0.5M$ (Figure 5-9). As the inclination changes from retrograde equatorial to prograde equatorial, the $\dot{e} = 0$ surface moves inwards to smaller p and also becomes closer to the innermost stable orbit.

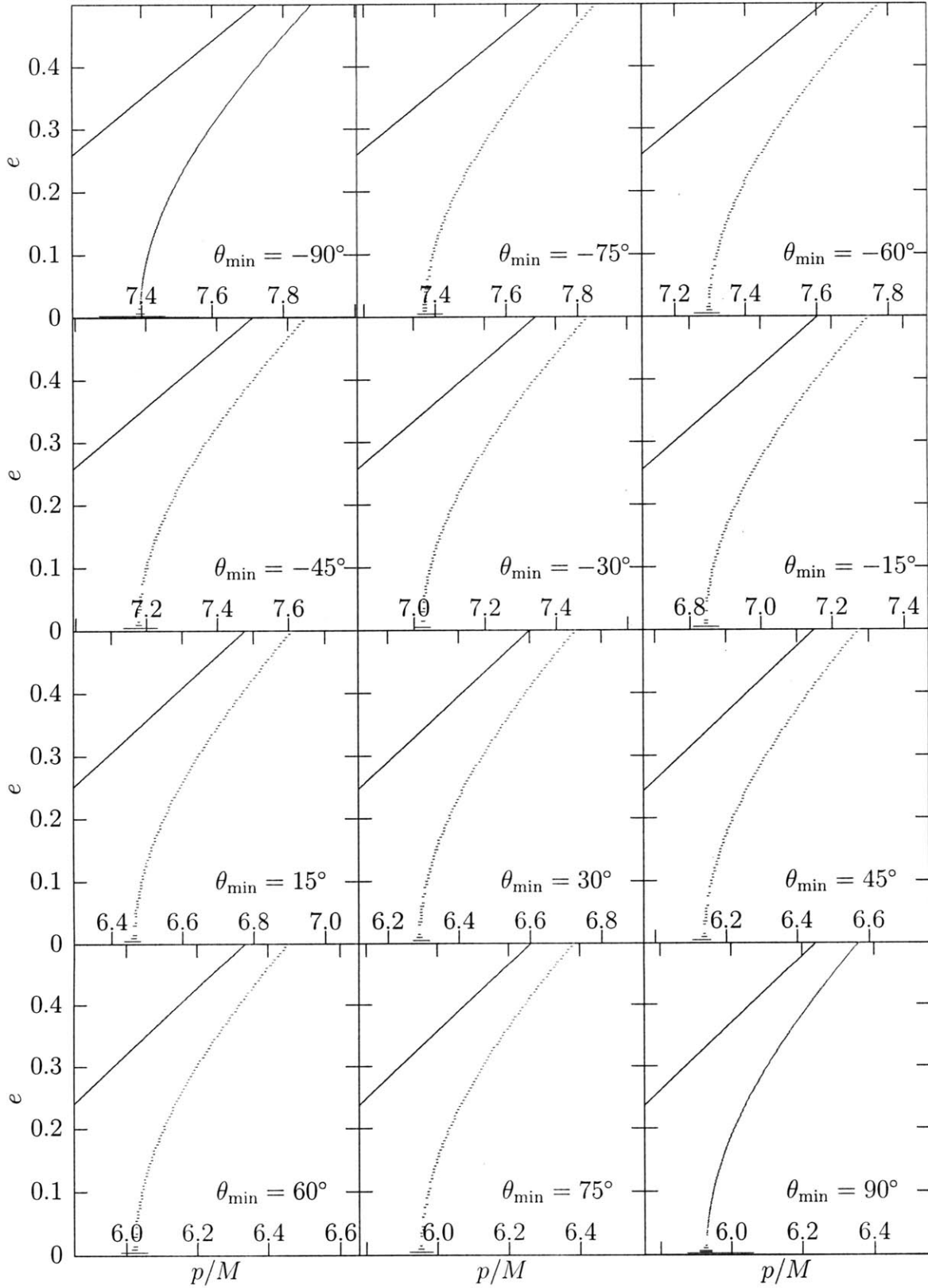


Figure 5-8: The curves $\dot{e} = 0$ for various inclination angles around a hole with spin $a = 0.2M$. The horizontal range on each plot is constant at 0.8.

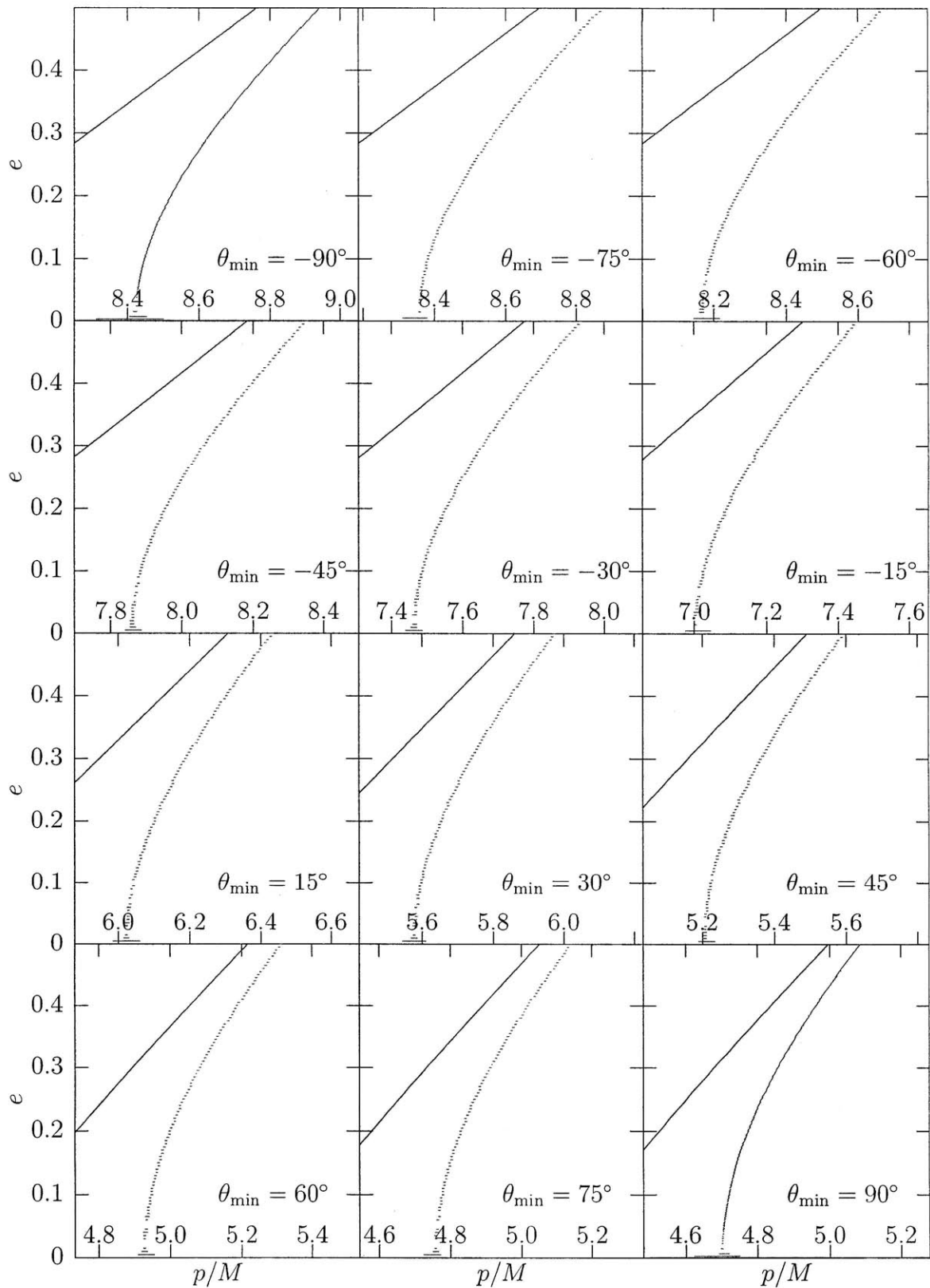


Figure 5-9: The curves $\dot{e} = 0$ for various inclination angles around a hole with spin $a = 0.5M$. The horizontal range on each plot is constant at 0.8.

Chapter 6

Conclusions and Future Work

I have presented here the results of implementing numerical code to evaluate gravitational wave fluxes using the numerical MST formalism developed by Fujita and Tagoshi. This code was then used to calculate the evolution of generic orbits in strong field regimes and compute the location of the surface dividing the large r circularizing evolution from the small r evolution towards increasing eccentricity.

The accuracy of evaluations of the Teukolsky solutions using Fujita and Tagoshi's method was found to be far superior to the accuracy obtained using the Sasaki-Nakamura transform. The fluxes obtained using the numerical MST method were found to agree with previous calculations to the claimed level of accuracy of the previous results.

The natural next step in this work is to employ the code to locate the $\dot{e} = 0$ surface at higher black hole spins than the two considered here. Comparison of fluxes for specific high spin orbits with previous results suggests that the code used here will be able to handle the higher spin cases without significant modification.

A more difficult project would be extending the known location of the surface to higher eccentricity orbits than the upper bound of 0.5 used here. For higher eccentricities, the number of Fourier modes required to approximate the fluxes well starts becoming prohibitively large: many of the calculations for the current work required 50–100,000 harmonics, of which half could be obtained by symmetry.

Appendix A

Orbital Details

For a particle at Boyer-Lindquist position $z^\mu = (t, r, \theta, \varphi)$ moving with 4-momentum $\mu(dz^\mu/d\tau) = (p^t, p^r, p^\theta, p^\varphi)$ for τ the proper time, the dimensionless energy, angular momentum, and Carter constant are constants of motion given by [12]

$$E = \frac{1}{\mu} \left[\left(1 - \frac{2Mr}{\Sigma}\right) p^t + \frac{2Mar \sin^2 \theta}{\Sigma} p^\varphi \right] \quad (\text{A.1})$$

$$L = \frac{1}{\mu M} \left[-\frac{2Mar \sin^2 \theta}{\Sigma} p^t + \frac{(r^2 + a^2)^2 - \Delta a^2 \sin^2 \theta}{\Sigma} \sin^2 \theta p^\varphi \right] \quad (\text{A.2})$$

$$Q = \frac{1}{\mu^2 M^2} \left[((\mu M L)^2 - a^2 (\mu E)^2 \sin^2 \theta) \cot^2 \theta + \Sigma^2 (p^\theta)^2 + \mu^2 a^2 \cos^2 \theta \right] \quad (\text{A.3})$$

where the expressions in square brackets are the dimensionful versions. The expression for Q has been simplified using the relation $p^2 = -\mu^2$.

The functions occurring in (1.9) are given by

$$V_r(r) = \mu^2 \left[(E(r^2 + a^2) - MaL)^2 - \Delta (r^2 + (ML - aE)^2 + M^2Q) \right] \quad (\text{A.4})$$

$$V_\theta(\theta) = \mu^2 \left[M^2Q - M^2L^2 \cot^2 \theta - a^2 (1 - E^2) \cos^2 \theta \right] \quad (\text{A.5})$$

$$V_t(r, \theta) = \mu \left[E \left(\frac{(r^2 + a^2)^2}{\Delta} - a^2 \sin^2 \theta \right) + MaL \left(1 - \frac{r^2 + a^2}{\Delta} \right) \right] \quad (\text{A.6})$$

$$V_\varphi(r, \theta) = \mu \left[ML \csc^2 \theta + aE \left(\frac{r^2 + a^2}{\Delta} - 1 \right) - \frac{Ma^2L}{\Delta} \right] \quad (\text{A.7})$$

and the Mino time parameter λ is defined by $d\tau/d\lambda = \mu\Sigma$.

The orbital parametrizations p, e, θ_{\min} and E, L, Q are most easily related by the implicit equations

$$0 = V_r \left(\frac{p}{1 \pm e} \right) \tag{A.8}$$

$$0 = V_\theta(\theta_{\min}), \tag{A.9}$$

which are easily seen from (1.9) and the fact that r_{\min} , r_{\max} , and θ_{\min} are turning points of the radial and angular motion.

Appendix B

Expressions for MST Quantities

The MST formalism provides two expressions for each of the independent solutions to the Teukolsky equation, and these can each be transformed using hypergeometric function identities into several useful forms. In the formulas below for R^{in} and R^{up} , the expressions in terms of Gauss hypergeometric functions (${}_2F_1(\cdot, \cdot; \cdot; \cdot)$) or R_0^ν are formally convergent for $r < \infty$ and expressions in terms of confluent hypergeometric functions (${}_1F_1(\cdot; \cdot; \cdot)$ and $U(\cdot, \cdot, \cdot)$) or R_C^ν are formally convergent for $r > r_+$, although their ranges of numerical usefulness are smaller. The ingoing solution can be expressed as

$$R^{\text{in}} = e^{i\epsilon\kappa x} (-x)^{-s-i(\epsilon+\tau)/2} (1-x)^{i(\epsilon-\kappa)/2} \quad (\text{B.1})$$

$$\times \sum_{n=-\infty}^{\infty} f_n^\nu {}_2F_1(n+\nu+1-i\tau, -n-\nu-i\tau; 1-s-i\epsilon-i\tau; x)$$

$$= e^{i\epsilon\kappa x} (-x)^{-s-i(\epsilon+\tau)/2} (1-x)^{-\nu-1+i(\epsilon+\tau)/2} \sum_{n=-\infty}^{\infty} f_n^\nu (1-x)^{-n} \quad (\text{B.2})$$

$$\times {}_2F_1\left(n+\nu+1-i\tau, n+\nu+1-s-i\epsilon; 1-s-i\epsilon-i\tau; \frac{-x}{1-x}\right)$$

$$= K_\nu R_C^\nu + K_{-\nu-1} R_C^{-\nu-1} \quad (\text{B.3})$$

$$= R_0^\nu + R_0^{-\nu-1}. \quad (\text{B.4})$$

Expressions (B.1) and (B.2) are termwise equal. Numerically, (B.2), (B.3), and (B.4) were found to be useful forms.

The upgoing solution is

$$R^{\text{up}} = 2^\nu z^{\nu-s} \left(1 - \frac{\epsilon\kappa}{z}\right)^{-s-i(\epsilon+\tau)/2} e^{iz-\pi\epsilon-i\pi(\nu+1+s)} \quad (\text{B.5})$$

$$\begin{aligned} & \times \sum_{n=-\infty}^{\infty} f_n^\nu(2iz)^n \frac{(\nu+1+s-i\epsilon)_n}{(\nu+1-s+i\epsilon)_n} U(n+\nu+1+s-i\epsilon, 2n+2\nu+2, -2iz) \\ & = 2^\nu z^{\nu-s} \left(1 - \frac{\epsilon\kappa}{z}\right)^{-s-i(\epsilon+\tau)/2} e^{iz-\pi\epsilon-i\pi(\nu+1+s)} (-2iz)^{-2\nu-1} \end{aligned} \quad (\text{B.6})$$

$$\begin{aligned} & \times \sum_{n=-\infty}^{\infty} f_n^\nu(2iz)^{-n} \frac{(\nu+1+s-i\epsilon)_n}{(\nu+1-s+i\epsilon)_n} U(-n-\nu+s-i\epsilon, -2n-2\nu, -2iz) \\ & = \frac{e^{-\pi\epsilon-i\pi s}}{\sin(2\pi\nu)} \left(\frac{e^{-i\pi\nu} \sin(\pi(\nu-s+i\epsilon))}{K_\nu} R_0^\nu - \frac{i \sin(\pi(\nu+s-i\epsilon))}{K_{-\nu-1}} R_0^{-\nu-1} \right) \end{aligned} \quad (\text{B.7})$$

where U is the Tricomi confluent hypergeometric function. As in the case of R^{in} , (B.5) and (B.6) are termwise equal, and in fact a useful expression for numerical calculation takes the negative n terms from (B.5) and the positive n terms from (B.6). This is useful because evaluation of hypergeometric functions is performed by summing a series which, particularly for large values of the function, often has large cancellations. As the result is generally more accurate when it is larger, and the two expressions are termwise equal, it is advantageous to take terms with prefactors that decrease with $|n|$. The expression (B.7) was also found to be numerically useful.

The additional Teukolsky solutions R_C^ν and R_0^ν are

$$R_C^\nu = e^{-iz} 2^\nu z^{\nu-s} \left(1 - \frac{\epsilon\kappa}{z}\right)^{-s-i(\epsilon+\tau)/2} \frac{\Gamma(\nu+1-s+i\epsilon)}{\Gamma(2\nu+2)} \quad (\text{B.8})$$

$$\times \sum_{n=-\infty}^{\infty} f_n^\nu(-2iz)^n \frac{(\nu+1+s-i\epsilon)_n}{(2\nu+2)_{2n}} {}_1F_1(n+\nu+1-s+i\epsilon; 2n+2\nu+2; 2iz)$$

$$R_0^\nu = e^{i\epsilon\kappa x} (-x)^{-s-i(\epsilon+\tau)/2} (1-x)^{\nu+i(\epsilon+\tau)/2} \frac{\Gamma(1-s-i\epsilon-i\tau)\Gamma(2\nu+1)}{\Gamma(\nu+1-i\tau)\Gamma(\nu+1-s-i\epsilon)} \quad (\text{B.9})$$

$$\begin{aligned} & \times \sum_{n=-\infty}^{\infty} f_n^\nu(1-x)^n \frac{(2\nu+1)_{2n}}{(\nu+1-i\tau)_n (\nu+1-s-i\epsilon)_n} \\ & \quad \times {}_2F_1\left(-n-\nu-i\tau, -n-\nu+2-i\epsilon; -2n-2\nu; \frac{1}{1-x}\right). \end{aligned}$$

By expanding both of these solutions in powers of $1-x = z/\epsilon\kappa$ at large radii, it can be seen that they are actually the same solution up to a constant (in r) factor, so we

then write $R_0^\nu = K_\nu R_C^\nu$, where

$$\begin{aligned}
K^\nu &= 2^{-s} (2\epsilon\kappa)^{s-\nu} e^{i\epsilon\kappa} \frac{\Gamma(1-s-i\epsilon-i\tau)\Gamma(2\nu+2)\Gamma(2\nu+1)}{\Gamma(\nu+1-s+i\epsilon)\Gamma(\nu+1-s-i\epsilon)\Gamma(\nu+1-i\tau)} \\
&\times \left(\sum_{n=0}^{\infty} f_n^\nu \frac{(-1)^n (2\nu+1)_n (\nu+1+s+i\epsilon)_n (\nu+1+i\tau)_n}{n! (\nu+1-s-i\epsilon)_n (\nu+1-i\tau)_n} \right) \\
&\times \left(\sum_{n=-\infty}^0 f_n^\nu \frac{(-1)^n (\nu+1+s-i\epsilon)_n}{(-n)! (2\nu+2)_n (\nu+1-s+i\epsilon)_n} \right)^{-1}. \quad (\text{B.10})
\end{aligned}$$

By taking the limits of the above expressions near the horizon and for large r and comparing with the asymptotic behaviors in (2.4) and (2.5), we can find expressions for the asymptotic amplitudes¹

$$B^{\text{trans}} = \left(\frac{\epsilon\kappa}{\omega}\right)^{2s} e^{i\kappa(\epsilon+\tau)\left(\frac{1}{2}+\frac{\log\kappa}{1+\kappa}\right)} \sum_{n=-\infty}^{\infty} f_n^\nu \quad (\text{B.11})$$

$$B^{\text{inc}} = \omega^{-1} e^{-i\epsilon(\log\epsilon-(1-\kappa)/2)} \left(K_\nu - i e^{-i\pi\nu} \frac{\sin(\pi(\nu-s+i\epsilon))}{\sin(\pi(\nu+s-i\epsilon))} K_{-\nu-1} \right) A_+^\nu \quad (\text{B.12})$$

$$B^{\text{ref}} = \omega^{-1-2s} e^{-i\epsilon(\log\epsilon-(1-\kappa)/2)} (K_\nu + i e^{i\pi\nu} K_{-\nu-1}) A_-^\nu \quad (\text{B.13})$$

$$C^{\text{trans}} = \omega^{-1-2s} e^{-i\epsilon(\log\epsilon-(1-\kappa)/2)} A_-^\nu \quad (\text{B.14})$$

where

$$A_+^\nu = 2^{-1+s-i\epsilon} e^{-\pi(\epsilon-i(\nu+1-s))/2} \frac{\Gamma(\nu+1-s+i\epsilon)}{\Gamma(\nu+1+s-i\epsilon)} \sum_{n=-\infty}^{\infty} f_n^\nu \quad (\text{B.15})$$

$$A_-^\nu = 2^{-1-s+i\epsilon} e^{-\pi(\epsilon+i(\nu+1+s))/2} \sum_{n=-\infty}^{\infty} f_n^\nu (-1)^n \frac{(\nu+1+s-i\epsilon)_n}{(\nu+1-s+i\epsilon)_n}. \quad (\text{B.16})$$

¹The phases of these expressions are incorrect almost everywhere in the literature.

Appendix C

List of Symbols

$(x)_n$	Pochhammer symbol $\Gamma(x+n)/\Gamma(x)$
a	Black hole spin (1.6)
α_n^ν	Coefficient in the recurrence for f_n^ν (3.5)
α_{lmkn}	Coefficient in ingoing flux equations (2.14)
$B^{\text{inc,ref,trans}}$	Ingoing asymptotic amplitudes (2.4)
β_n^ν	Coefficient in the recurrence for f_n^ν (3.6)
$C^{\text{ref,trans,up}}$	Upgoing asymptotic amplitudes (2.5)
Δ	$r^2 - 2Mr + a^2 = (r - r_+)(r - r_-)$ (1.6)
E	Energy of an orbiting particle
\dot{E}	Energy removed from particle $-dE/dt$ (superscript H or ∞ can indicate direction)
e	Orbital eccentricity (1.8)
ϵ	$2M\omega$ (3.1)
${}_pF_q$	Hypergeometric function
f_n^ν	Coefficients in MST expansions (3.1)
$g_n(\nu)$	Continued fraction function (3.14)
Γ	Mino time average of $dt/d\lambda$ (1.9)
γ_n^ν	Coefficient in the recurrence for f_n^ν (3.7)
$h_{+,x}$	Gravitational wave amplitudes

K	$(r^2 + a^2)\omega - am$ (2.3)
K_ν	Constants occurring in various MST formulas (B.10)
k	θ index on Teukolsky and related functions (1.11)
κ	$\sqrt{1 - q^2}$ (3.1)
L	z -angular momentum of an orbiting particle
\dot{L}	Angular momentum removed from particle $-dL/dt$ (superscript H or ∞ can indicate direction)
l	principal index on Teukolsky and related functions (2.1)
λ	Eigenvalue of the angular Teukolsky equation (2.3)
λ	Mino time parameter (1.9)
M	Black hole mass (1.6)
m	φ index on Teukolsky and related functions (1.11), (2.1)
μ	Mass of the orbiting body
n	r index on Teukolsky and related functions (1.11)
ν	Renormalized angular momentum
$\Omega_{r,\theta,\varphi}$	Boyer-Lindquist time orbital frequencies $\Upsilon_{r,\theta,\varphi}/\Gamma$ (1.10)
ω	Mode frequency (2.1)
P	$\omega - ma/2Mr_+$ (2.4)
p	Orbital semilatus rectum (1.8)
φ	Boyer-Lindquist azimuth (1.6)
ψ	Full Teukolsky function (2.1)
Q	Carter constant of an orbiting particle
\dot{Q}	Carter constant removed from particle $-dQ/dt$ (superscript H or ∞ can indicate direction)
q	a/M nondimensionalized spin (1.6)
R	Radial Teukolsky function (2.1)
R'_0	$K_\nu R'_C$, but used to indicate computation using (B.9)
R'_C	“Coulomb” Teukolsky solution (B.8)
R^{in}	Ingoing Teukolsky solution (2.4)
R^{up}	Upgoing Teukolsky solution (2.5)

r	Boyer-Lindquist radius (1.6)
r_{\pm}	$M \pm \sqrt{M^2 - a^2}$ (r_+ is the horizon radius) (1.6)
$r_{\min, \max}$	Radial turning points of a bound orbit (1.8)
r^*	tortoise coordinate (2.6)
ρ	$-1/(r - ia \cos \theta)$ (2.8)
S	Spin-weighted spheroidal harmonic (2.1)
s	Field spin weight (-2 for gravitational waves) (2.2)
Σ	$r^2 + a^2 \cos^2 \theta$ (1.6)
\mathcal{T}	Teukolsky source (2.2)
t	Boyer-Lindquist time (1.6)
τ	$(\epsilon - m\eta)/\kappa$ (3.1)
θ	Boyer-Lindquist inclination (1.6)
θ_{\min}	Orbital inclination
U	Tricomi confluent hypergeometric function
$\Upsilon_{r, \theta, \varphi}$	Mino time orbital frequencies (1.9)
V	Teukolsky potential (2.3)
x	$\omega(r_+ - r)/\epsilon\kappa$ (3.1)
Z^H	Coefficient of R^{up} in the radiated field at infinity (2.11)
Z^{∞}	Coefficient of R^{in} in the radiated field at the horizon (2.14)
z	$\omega(r - r_-)$ (3.1)

Bibliography

- [1] Sean M. Carroll. *Spacetime and Geometry*. Addison Wesley, 2004.
- [2] Steve Drasco and Scott A. Hughes. Gravitational wave snapshots of generic extreme mass ratio inspirals. *Phys. Rev. D*, 73:024027, 2006.
- [3] Ryuichi Fujita and Hideyuki Tagoshi. New numerical methods to evaluate homogeneous solutions of the Teukolsky equation. *Prog. Theor. Phys.*, 112(3):415–450, 2004.
- [4] Ryuichi Fujita and Hideyuki Tagoshi. New numerical methods to evaluate homogeneous solutions of the Teukolsky equation. II. *Prog. Theor. Phys.*, 113(6):1165–1182, 2005.
- [5] Kostas Glampedakis and Daniel Kennefick. Zoom and whirl: Eccentric equatorial orbits around spinning black holes and their evolution under gravitational radiation reaction. *Phys. Rev. D*, 66:044002, 2002.
- [6] Scott A. Hughes. Evolution of circular, nonequatorial orbits of Kerr black holes due to gravitational-wave emission. *Phys. Rev. D*, 61:084004, 2000.
- [7] Richard A. Isaacson. Gravitational radiation in the limit of high frequency. II. nonlinear terms and the effective stress tensor. *Phys. Rev.*, 166(5):1272–1280, 1968.
- [8] Daniel Kennefick and Amos Ori. Radiation-reaction-induced evolution of circular orbits of particles around Kerr black holes. *Phys. Rev. D*, 53:4319–4326, 1996.
- [9] Shuhei Mano, Hisao Suzuki, and Eiichi Takasugi. Analytic solutions of the Teukolsky equation and their low frequency expansions. *Prog. Theor. Phys.*, 95(6):1079–1096, 1996.
- [10] Yasushi Mino. Perturbative approach to an orbital evolution around a supermassive black hole. *Phys. Rev. D*, 67:084027, 2003.
- [11] William H. Press, Saul A. Teukolsky, William T. Vetterling, and Brian P. Flannery. *Numerical Recipes in C++*. Cambridge University Press, second edition, 2002.

- [12] Norichika Sago, Takahiro Tanaka, Wataru Hikida, and Hiroyuki Nakano. Adiabatic radiation reaction to orbits in Kerr spacetime. *Prog. Theor. Phys.*, 114(2):509–514, 2005.
- [13] Misao Sasaki and Takashi Nakamura. Gravitational radiation from a Kerr black hole. I. *Prog. Theor. Phys.*, 67(6):1788–1809, 1982.
- [14] Saul A. Teukolsky. Perturbations of a rotating black hole. I. fundamental equations for gravitational, electromagnetic, and neutrino-field perturbations. *Astrophys. J.*, 185:635–647, 1973.
- [15] Saul A. Teukolsky and William H. Press. Perturbations of a rotating black hole. III. interaction of the hole with gravitational and electromagnetic radiation. *Astrophys. J.*, 193:443–461, 1974.